1   Structures in multiple conformations reveal distinct transition metal and proton pathways in an

2   Nramp transporter

3

4   Aaron T. Bozzi[1,3], Christina M. Zimanyi[1,2,3], John M. Nicoludis[1], Brandon K. Lee[1], Casey H.

5   Zhang[1], and Rachelle Gaudet[1,*]

6

7   [1]Department of Molecular and Cellular Biology, Harvard University, 52 Oxford Street,

8   Cambridge, MA 02138, USA

9   [2]Current address: New York Structural Biology Center, 89 Convent Ave., New York, NY 10027,

10   USA

11   [3]Co-first author

12   *Corresponding author

13 **Abstract**

14   Nramp family transporters—expressed in organisms from bacteria to humans—enable uptake of

15   essential divalent transition metals via an alternating-access mechanism that includes proton co-

16   transport. We present high-resolution structures of *Deinococcus radiodurans* (Dra)Nramp at

17   complementary stages of its transport cycle to provide a thorough description of the Nramp

18   transport cycle by identifying the key intramolecular rearrangements and changes to the metal

19   coordination sphere. Strikingly, while metal transport requires cycling from outward- to inward-

20   open states, efficient proton transport still occurs in outward-locked (but not inward-locked)

21   DraNramp. We propose a model in which metal and proton enter the transporter via the same

22   external pathway to the binding site, but follow separate routes to the cytoplasm, thus resolving

23   the electrostatic dilemma of using a cation co-substrate to drive a cation primary substrate. Our

24   results illustrate the flexibility of the LeuT fold to support a broad range of co-substrate coupling

25   and conformational change mechanisms.

26   **Introduction**

27   The amino acid-polyamine-organocation (APC) superfamily of secondary transporters

28   encompasses a broad range of evolutionarily-related proteins that transport diverse substrates

29   including neurotransmitters, metabolites, and transition metals in organisms throughout the tree of

30   life (Vastermark et al., 2014; Wong et al., 2012). In humans alone, the APC superfamily

31   encompasses 11 subfamilies of distinct solute carrier proteins (Perland and Fredriksson, 2017).

32   These transporters harness the energy stored in preexisting transmembrane ion gradients. The

33   LeuT fold (Yamashita et al., 2005) is the core structural unit that undergoes conformational

34   rearrangements necessary for alternating access-based transport in the APC superfamily. This fold

35   consists of ten transmembrane (TM) segments, divided into two pseudosymmetric, interlocking

36   five-TM repeats, although many members have additional TMs. Primary substrates bind in a

37   pocket formed by non-helical regions of TM1 and TM6, close to the center of the membrane. Co-

38   transported coupling ions—typically Na^+ and/or H^+—bind at the interface between two proposed

39   domains (Perez and Ziegler, 2013; Rudnick, 2013): a "bundle" formed by TMs 1, 2, 6, and 7; and

40   a "scaffold" or "hash" domain comprising most or all of the remaining six TMs (Forrest and

41   Rudnick, 2009). When all substrates are bound, conformational rearrangement closes an external

42   vestibule between "bundle" and "scaffold" and opens an intracellular vestibule between the two

43   domains to allow substrate release (Boudker and Verdon, 2010; Forrest et al., 2011; Shi, 2013).

44   Despite the common fold, many APC members have little-to-no sequence identity, consistent with

45   mechanistic divergences, including variance in the identity and stoichiometry of the coupled ions

46   (Ma et al., 2012; Shaffer et al., 2009) and in which helices move the most to open and close the

47   inner and outer gates (Kazmier et al., 2017; Kazmier et al., 2014a; Kazmier et al., 2014b;

48   Krishnamurthy and Gouaux, 2012; Malinauskaite et al., 2014; Ressl et al., 2009; Shimamura et

49   al., 2010; Weyand et al., 2008).

50   Natural resistance-associated macrophage proteins (Nramps) are APC-superfamily transition

51   metal transporters that enable uptake of rare micronutrients such as Mn^{2+} in plants and bacteria

52   and Fe^{2+} in animals (Cellier, 2012; Courville et al., 2006; Nevo and Nelson, 2006). Nramps bind

53   and/or transport biologically essential divalent metals such as Mn^{2+}, Fe^{2+}, Co^{2+}, Ni^{2+}, Cu^{2+}, Zn^{2+}—

54   and toxic metals like Cd^{2+}, Pb^{2+}, and Hg^{2+}—but not the abundant alkaline earth metals Mg^{2+} and

55   Ca^{2+} (Bozzi et al., 2016a; Ehrnstorfer et al., 2014). Metal uptake by Nramps involves proton co-

56   transport, and many homologs also display considerable proton uniport—proton transport in the

57   absence of added metal that suggests loose coupling between the co-substrates (Chen et al., 1999;

58   Gunshin et al., 1997; Mackenzie et al., 2006; Nelson et al., 2002; Xu et al., 2004). Nramps have

59   11 or 12 TMs, the first ten forming a LeuT fold, as seen in structures of three bacterial Nramp

60   homologs (Bozzi et al., 2016b; Ehrnstorfer et al., 2014; Ehrnstorfer et al., 2017), including our

61   model system *Deinococcus radiodurans* (Dra)Nramp (Bozzi et al., 2016b). Conserved aspartate,

62   asparagine, and methionine residues in TM1 and TM6 coordinate transition metal substrates as

63   observed in an inward-open state (Ehrnstorfer et al., 2014), while only a metal-free outward-open

64   state has been reported (Ehrnstorfer et al., 2017).

65   Here we provide the first complementary structures of the same Nramp homolog in multiple

66   conformations, including the first metal-bound outward-open Nramp structure, and a novel

67   inward-occluded structure. These allow us to fully illustrate the transport cycle for DraNramp. We

68   also show that metal transport requires the expected alternating access bulk conformational

69   change, whereas proton transport can occur via a more channel-like mechanism in the outward-

70   open state. Using the structures and accompanying biochemical data, we delineate separate

4

71   conserved transport pathways for metal and proton substrates and provide a mechanistic model

72   encompassing substrate binding, release, and the conformational change process. We demonstrate

73   novel modes of conformational rearrangement and ion shuttling in DraNramp compared to other

74   LeuT-fold transporters, thus expanding the known repertoire of intramolecular dynamics and

75   coupling mechanisms possible within this important protein family.

76

77   **Results**

78   **Rational design and validation of conformationally-locked DraNramp constructs**

79   A previously determined structure of a Fab-bound DraNramp in an inward-open conformation

80   revealed the intracellular metal permeation pathway, or vestibule, between TMs 1a, 2, 5, 6b, 7,

81   and 8 (Bozzi et al., 2016b). This structure was stabilized in an inward-open state by patches of

82   mutations to intracellular loops 4-5, 6-7, and 10-11, and we thus refer to it as the Patch mutant. To

83   observe additional conformational states of a transport cycle in a single Nramp homolog at high

84   resolution, we developed two complementary conformationally-locked constructs for

85   crystallization. Adding steric bulk along TM1a—for example a G45R mutation, which mimics a

86   human anemia-causing mutation of a conserved glycine (Barrios et al., 2012)—prevented full

87   closing of the intracellular vestibule and eliminated metal transport, emphasizing the importance

88   of the alternating-access mechanism to DraNramp function(Bozzi et al., 2016b). Based on these

89   findings we pursued the G45R mutant as a new inward-locked crystallization construct.

90   To develop a complementary outward-locked DraNramp construct, we adapted an approach

91   previously described for the lactose transporter LacY (Kumar et al., 2014; Smirnova et al., 2013).

92   By mapping extensive cysteine accessibility data onto the inward-open structure, we identified the

93   external vestibule between TMs 1b, 6a, 3, 8, and 10 (Bozzi et al., 2016b). We created a panel of

5

94   11 tryptophan point mutants lining this predicted external vestibule (Figure 1A) to destabilize the

95   inward-open state. An outward-locking mutation should severely impair metal transport, and

96   indeed several mutants had impaired *in vivo* Co^{2+} uptake when expressed in *Escherichia coli*

97   (Figure 1B and Figure 1—figure supplement 1A). We chose to pursue G223W—on TM6a one

98   helical turn above the unwound metal-binding region—which like G45R eliminated Co^{2+} and Fe^{2+}

99   metal transport (Figure 1—figure supplement 1B). Importantly, while a tryptophan modeled in the

100 inward-open state at position 223 clashes with the top of TM10, the analogous glycine position in

101 the recent structure of outward-open *Eremococcus coleocola* (Eco)Nramp (33% identity with

102 DraNramp) lines a wide aqueous channel with adequate room for tryptophan's bulk (Ehrnstorfer

103 et al., 2017).

104

105 To further validate this G223W construct, we measured bulk solvent accessibility of two single-

106 cysteine reporters: A61C on TM1b, which is only exposed in DraNramp's outward-open state

107 (Bozzi et al., 2016b); and A53C on TM1a just below the metal-binding D56, a putative inward-

108 open reporter based on comparing the Patch mutant and EcoNramp structures (Figure 1C and

109 Figure 1—figure supplement 1C). WT-like DraNramp (with the indicated reporter cysteine and a

110 C382S mutation to remove the lone endogenous cysteine) maintains a dynamic conformational

111 equilibrium—even in the absence of added metal substrate—such that either reporter can be fully

112 modified by the thiol-specific N-ethylmaleimide (NEM) at high concentrations (Figure 1D-E).

113 G45R slightly increased A53C accessibility but fully protected A61C, indicating an inward-locked

114 state, while G223W slightly increased A61C accessibility while fully protecting A53C, consistent

115 with an outward-locked state (Figure 1D-E and Figure 1—figure supplement 1D). We have thus

116 identified two complementary constructs that trap DraNramp in outward-locked (G223W) and

117   inward-locked (G45R) states (Figure 2—figure supplement 2A). Using lipidic cubic phase (LCP)

118   to mimic the hydrophobic membrane environment, we crystallized and determined the structures

119   of G45R and G223W to resolutions of 3.0 and 2.4 Å, respectively, both significantly improved

120   from our earlier DraNramp structure (3.94 Å) (Table 1 and Figure 2—figure supplements 1-2).

121   The new high-resolution structures also allowed us to re-refine our original structure, including

122   correction of a sequence registry error in TM11.

123

124   **Structure of G45R DraNramp reveals inward-occluded state**

125   Unexpectedly, the G45R structure is not in an inward-open conformation as seen previously with

126   our Fab-bound Patch mutant (Figure 2A) but instead adopts an inward-occluded, metal-free state

127   (Figure 2B) that may represent an intermediate conformation between inward-open and outward-

128   open states in the DraNramp transport cycle (Figure 2D). As in the inward-open apo state, the

129   external vestibule remains sealed, with TM1b and TM6a forming tight hydrophobic packing with

130   the tops of TM3 and TM10, and most TMs undergo little apparent displacement (Figure 2F-G).

131   The major exception is TM1a, which swings ~45° to partially seal the inward aqueous cavity in

132   the G45R structure, a motion we previously showed to be essential to the transport cycle (Bozzi et

133   al., 2016b). The intracellular ends of TM4 and TM5 also move slightly compared to their position

134   in the inward-open state, further sealing the metal-binding site from the cytosol. Comparisons of

135   the G45R and G223W structures indicate that, rather than preventing inward motion of TM1a as

136   we had hypothesized (Bozzi et al., 2016b), the G45R mutation precludes TM4-TM5 from fully

137   closing the inner gate, as any bulkier replacement for that absolutely-conserved glycine in our

138   outward-open G223W structure would clash with E176 on TM5. Consequently, the intracellular

139   vestibule to the metal-binding site is highly constricted yet there is no aqueous pathway to the

140 binding site from the external side (Figure 2B). Structural alignments with the inward-open

141 *Staphylococcus capitis* (Sca)Nramp (Ehrnstorfer et al., 2014) and outward-open EcoNramp

142 (Ehrnstorfer et al., 2017) also indicate an intermediate conformation for the G45R structure, albeit

143 closer to the inward-open state (Figure 2E and Figure 2—figure supplement 2D), confirming our

144 assignment as inward-occluded.

145

146 **Structure of G223W DraNramp provides first metal-bound outward-open state**

147 The G223W structure represents an outward-open, metal-bound state that superimposes best with

148 the outward-open EcoNramp structure (Figure 2E and Figure 2—figure supplement 2E). As

149 predicted, the exogenous tryptophan lines a periplasmic-facing aqueous cavity leading to a bound

150 Mn^{2+} in the center of the transporter, with tight helix packing below precluding metal passage to

151 the cytoplasm. We also determined a G223W apo structure (Table 1—table supplement 1), which

152 lacks electron density attributable to metal substrate in the binding site (Figure 2—figure

153 supplement 2C) but is otherwise similar to the metal-bound state (Cα RMSD = 1.08 Å); hence we

154 used the metal-bound structure for all further analyses. Compared to the inward-open and inward-

155 occluded structures, in the outward-open state TM1b, TM6a, and the top of TM10 are splayed

156 open, and loop 1-2 is displaced by ~4 Å, to form a wide aqueous pathway to the metal-binding site

157 (Figure 2H-I). On the cytoplasmic side, TM4 and TM5 move significantly (by ~8 Å) straddling

158 TM8 and approaching TM1a, while TM1a also approaches TM8 to fully shut the interior aqueous

159 vestibule (Figure 2H-I).

160

161 **Comparisons of DraNramp structures define a scaffold and flexible regions**

162   Based on overall superpositions of the three DraNramp structures, TMs 1, 4, 5, 6, and 10 show the

163   largest displacements to switch metal-binding site accessibility (Figure 2F-I). The remaining TMs

164   (2, 3, 7, 8, 9, and 11) would thus form a "scaffold," which adjusts to accommodate the more

165   significant movements of the other five TMs (Video 1).

166   To more objectively compare the intramolecular rearrangements that occur during the transport

167   cycle, we calculated difference distance matrices (Richards and Kundrot, 1988), averaged by TM,

168   for each pair of structures (Figure 3). These matrices confirm that TMs 1, 4, 5, 6, and 10 undergo

169   the most significant displacements relative to the rest of the protein between the different

170   structures. But rather than moving as a rigid body such as proposed in the "rocking bundle" model

171   for LeuT (Forrest and Rudnick, 2009), these five TMs are also significantly displaced relative to

172   each other.

173

174   **The G223W outward-open structure reveals a metal-coordination sphere distinct from the**

175   **inward-open state's**

176   Like other LeuT-family members, DraNramp relies on unwound regions of its TMs to bind

177   substrates. A conserved DPGN sequence is non-helical in TM1—with the helix-breaking proline-

178   glycine pair separating two metal-binding residues—while a conserved MPH sequence that

179   includes the metal-binding methionine ends an unwound region in TM6 (Figure 4A-C). We used

180   these two canonical motifs to generate an alignment of 6878 Nramp sequences (Figure 2—source

181   data 1) and calculate the conservation of other important residues (Figure 2—figure supplement

182   1C). Interestingly, a third proline, P386 (83% conserved), enables the top of TM10 to swing to

183   open the metal-binding site from the periplasm, while T228 (80%) on TM6 and N426 (99%) on

9

184   TM11 stabilize the extended unwound TM6 region in the G223W structure (Figure 4—figure

185   supplement 1A).

186   The inward-open ScaNramp structure revealed a metal-binding site consisting of three conserved

187   sidechains corresponding to D56, N59, and M230 in DraNramp, and a backbone carbonyl of A227

188   (Figure 4B) (Ehrnstorfer et al., 2014). In outward-open DraNramp, a Mn^{2+} binds both D56 and

189   M230 (2.9 and 3.0 Å), with N59 slightly further away (3.4 Å) (Figure 4A). The increased

190   unwinding of TM6a displaces the A227 carbonyl too far (6.5 Å) to coordinate the metal (Figure

191   4—figure supplement 1A-B). Instead, the A53 carbonyl coordinates the Mn^{2+} (2.0 Å)—our

192   structure is thus the first to implicate this residue in the metal transport cycle. Two waters (2.7 and

193   2.8 Å) complete a Mn^{2+}-coordination sphere. While the resolution remains too low to definitively

194   define the coordination geometry, the electron density is consistent with Mn^{2+} interacting with

195   both D56 oxygens and thus seven total ligands—rare but not unprecedented for Mn^{2+} (Barber-

196   Zucker et al., 2017; Glasfeld et al., 2003). An ordered water network expands into the external

197   vestibule as part of the extended metal coordination sphere (Figure 4—figure supplement 1A). A

198   water is also tethered to the conserved H232 directly below the metal-binding M230, perhaps

199   poised to hydrate the cation upon conformational change.

200

201   **The G45R inward-occluded structure suggests potential metal-binding role for conserved**

202   **Q378**

203   The inward-occluded G45R binding site contains no metal. The A53 carbonyl is farther from the

204   other metal-binding residues than the A227 carbonyl (Figure 4C). This is consistent with a model

205   in which Nramp metal transport involves a switch of ligands, perhaps with the A53 and A227

206   carbonyls both coordinating the metal substrate in an as-yet-uncaptured intermediate state.

10

207   In G45R, flexing of TM10 above its P386 pivot shifts Q378 (86%, 11% N) ~5 Å to within

208   hydrogen-bonding distance of metal-binding A227 and D56, perhaps stabilizing the negative

209   charge during the empty transporter's return to outward-open. While Q378 does not bind the metal

210   substrate in either outward DraNramp (7.9 Å) or inward ScaNramp(Ehrnstorfer et al., 2014) (4.5

211   Å), its position in the G45R occluded intermediate suggests it may transiently bind during the

212   transport process. Indeed, two independent molecular dynamics (MD) simulations of the inward-

213   open ScaNramp showed a metal interaction with the Q378 oxygen (Bozzi et al., 2016a; Pujol-

214   Gimenez et al., 2017), and mutations at this position impaired metal transport in HsNramp2 (Pujol-

215   Gimenez et al., 2017).

216   To test the importance of the three conserved sidechains that coordinate Mn^{2+} (D56, N59, and

217   M230; Figure 4A-B) and Q378 to metal transport, we purified a panel of mutants and reconstituted

218   them into proteoliposomes (Figure 4D). D56A and D56N eliminated Mn^{2+} and Cd^{2+} transport

219   (Figure 4E-F and Figure 4—figure supplement 1C-D), confirming the importance of D56. N59A

220   severely and N59D moderately reduced transport of both metals (Figure 4E-F and Figure 4—figure

221   supplement 1C-D). Both M230A and M230T transport both metal substrates (Figure 4—figure

222   supplement 1C-D), but with lower apparent affinity than WT (Figure 4E-F). Consistent with our

223   previous findings, removing M230—the lone sulfur-containing metal-binding residue—affects

224   Cd^{2+} more than Mn^{2+} transport, reflecting the importance of the semi-covalent interaction Cd^{2+} can

225   form with sulfur (Bozzi et al., 2016a). Lastly, Q378S and Q378N both preserved significant

226   transport of both metals (Figure 4—figure supplement 1C-D). However, these mutants notably

227   impaired transport at lower concentrations for Mn^{2+}—but interestingly not Cd^{2+} (Figure 4E-F).

228   That the native glutamine is essential for efficient transport of the biological substrate Mn^{2+} but

229   dispensable for Cd^{2+} uptake (Figure 4—figure supplement 1E) suggests that the two metals interact

230   differently with their surrounding ligands during the transport process, corroborating the

231   differential effects of M230 mutations.

232

DraNramp proton transport does not require large conformational change

234   We reconstituted G45R and G223W into proteoliposomes to assess their metal and proton

235   transport (Figure 5A). Consistent with our *in vivo* findings, neither G45R nor G223W transport

236   Mn^{2+}, Cd^{2+}, or Co^{2+} (Figure 5B and Figure 5—figure supplement 1A-B). Surprisingly, in the

237   presence of a favorable negative membrane potential, G223W enabled larger basal H^+ influx than

238   WT, while G45R had no H^+ flux (Figure 5C). Interestingly, while Mn^{2+} co-transport stimulated

239   H^+ uptake for WT, adding Mn^{2+} did not further stimulate either G45R or G223W (Figure 5C).

240   These results suggest that Nramp metal and proton transport proceed via separate routes, with

241   proton transport requiring only that the protein sample the outward-open state.

242   To test this new hypothesis, we reconstituted the A53C and A61C mutants, with single cysteines

243   located just below or above the metal-binding site respectively (Figure 5—figure supplement 1D).

244   Both retain significant metal transport (Figure 5E,G and Figure 5—figure supplement 1E-F), and

245   can be targeted with cysteine-specific modifiers to post-translationally add bulky and/or charged

246   wedges to impede conformational change (Figure 5D and Figure 5—figure supplement 1C).

247   Charged, and thus membrane-impermeable, MTSET nearly eliminated metal transport by A61C,

248   while uncharged NEM or MTSEA moderately impaired or did not affect transport, respectively

249   (Figure 5E and Figure 5—figure supplement 1E), a result consistent with our previous *in vivo*

250   findings that adding steric bulk, but not formal charge, is tolerated at this position (Bozzi et al.,

251   2016b). In addition, MTSET-treated A61C replicated G223W's H^+-transport behavior, with higher

252   H^+ uniport compared to unmodified transporter, but little stimulation by Mn^{2+} (Figure 5F). In

12

253   contrast MTSET had no effect on Mn^{2+} and Cd^{2+} transport by A53C, but membrane-permeable

254   MTSEA and NEM both eliminated transport (Figure 5G and Figure 5—figure supplement 1F).

255   Regarding H^+ uptake, MTSEA- and NEM-treated A53C resembled G45R, with no basal uniport

256   or Mn^{2+} stimulation, while again unmodified and MTSET-treated A53C both behaved similarly to

257   WT (Figure 5H). These findings show that essentially all activity in proteoliposomes, which likely

258   contain a mix of inside-out and outside-out transporters, comes from outside-out DraNramp.

259   MTSET, which should inhibit any inside-out A53C, did not affect transport, indicating that inside-

260   out transporters contribute negligibly to the total activity, a result we more fully explore in an

261   accompanying paper (Bozzi et al., 2018). Consistently, while MTSET treatment spares inside-out

262   A61C from labeling, it nevertheless nearly eliminated metal transport.

263   In summary, these experiments with permanently-locked crystallization constructs or chemically-

264   locked cysteine mutants demonstrated that while metal transport requires complete conformational

265   cycling, proton transport does not require large-scale conformational change and can proceed

266   through DraNramp's outward-open state but not its inward-open state.

267

268   **Conserved salt-bridge network provides potential proton pathway to cytoplasm**

269   Our *in vitro* results suggested that proton transport occurs via a pathway separate from the

270   intracellular metal-release vestibule, which remains closed to bulk solvent in the proton-

271   transporting G223W mutant. Below the metal-binding site begins a network of highly-conserved

272   hydrophilic residues, including at least seven potentially protonatable sidechains, that leads from

273   the metal-binding D56 through a tight corridor between TMs 3, 4, 8, and 9 to the cytoplasm (Figure

274   6A-C). In contrast to the external and intracellular vestibules proposed as metal entrance and

13

275   release pathways, the helices and residues within this polar network undergo little rearrangement

276   between the three DraNramp structures, except the intracellular end of TM4 (Figures 2F-I and 3).

277   Highly-conserved residues surrounding the metal-binding D56 include H232 on TM6b (100% as

278   defined) and E134 (98%, TM3)—which have each been proposed as the Nramp proton transfer

279   point(Ehrnstorfer et al., 2017; Pujol-Gimenez et al., 2017). Across from E134 lies a conserved salt-

280   bridge pair: D131 (TM3, 93%) and R353 (TM9, 78%). Approximately 9 Å below, a second

281   conserved salt-bridge, E124-R352 (94% and 87%), links the same two helices. This network could

282   provide the route for proton uniport in the outward-open conformation.

283

284   **Two conserved aspartates anchor the DraNramp proton transport pathway**

285   To assess whether these residues could be proton carriers, we calculated predicted pK_a values for

286   our outward-open and inward-occluded structures (Figure 6D) (Dolinsky et al., 2004).

287   Surprisingly, D56 is the only residue with a pK_a in the ideal 6-7 range to facilitate proton exchange

288   at a typical external pH. About 4 Å from D56, E134's high pK_a indicates a near permanently-

289   protonated state, while H232—4 Å below E134 and 7 Å from D56—has too low a pK_a to easily

290   protonate, as does H237 further down TM6b. While E134 and H232 have separately been

291   suggested as the Nramp proton-binding site (Ehrnstorfer et al., 2017; Pujol-Gimenez et al., 2017),

292   our pK_a predictions suggest otherwise, as maintaining a formal change, especially on a histidine,

293   would not be favorable in the protein core, while the E-to-Q mutant at that position in EcoNramp

294   maintained WT-like proton transport ability (Ehrnstorfer et al., 2017), which argues against that

295   residue as an essential transfer point. Within the TM3-TM9 salt-bridge network, R352 and R353

296   are likely protonated and positively charged, while their respective partners E124 and D131 are

297   likely deprotonated and negatively charged. The predicted pK_a values of D131 and E124 indicate

14

298   their amenability to protonation. Indeed, as D56's predicted pK_a drops to 3.2 with Mn^{2+} bound,

299   D131 becomes the best candidate to receive a proton.

300   We observed three distinct voltage-driven H^+ transport phenotypes within a panel of mutants to

301   highly-conserved residues (Figure 6E and Figure 6—figure supplement 1). First, removing either

302   metal-binding residue N59 or M230 has little effect. Second, neutralizing any member of the D56-

303   E134-H232-D131 network or the H237Q mutation drastically reduced H^+ transport. Third,

304   mutating any of E124, R352, R353—farthest from D56—increased H^+ uniport across multiple

305   voltages.

306   Outward-reporter A61C accessibility (Figure 1C) is consistent with each mutant sampling the

307   outward-open state needed for proton transport (Figure 5), ruling out a conformation-locking

308   explanation for the loss-of-function mutants. While some mutations perturbed the transporter's

309   conformational preference, A61C remained at least somewhat accessible in all cases except

310   H237Q (Figure 6F).

311   In summary, D56 is the likely initial protonation point, with E134 and H232 positioned to

312   chaperone the proton transfer to D131, while R352, R353, and E124 restrain this process (Figure

313   6G).

314

315   **Discussion**

316   We propose a structure-based model for conformation cycling in DraNramp (Figure 7A-B).

317   Starting from the outward-open state seen in our G223W structure (Figure 7A, left panel), metal

318   binding and resulting proton entry into its release pathway may trigger bulk conformational

319   rearrangement (see below for details). To close the external vestibule, TM6a, TM10, and to a lesser

320   extent TM1b move inward above their respective non-helical hinge regions, with the TM6a

15

321   movement propagated through the TM5-6 linker, causing rigid rotation of TM5 to begin to open

322   the inner gate. From this transient occluded conformation similar to our G45R structure (Figure

323   7A, middle panel), additional movement of TM4-TM5 allows TM1a to bend upward to fully open

324   the inner gate, enabling solvent access to and release of the metal, as the protein achieves a state

325   similar to the Patch mutant DraNramp structure (Figure 7A, right panel) (Bozzi et al., 2016b).

326   Analogously, to return to the outward-open state and complete the transport cycle, TM1a swings

327   in to reach a conformation similar to G45R, then TM4-TM5 fully close on TM1a to seal the

328   cytoplasmic vestibule while TM1b, TM6a, and TM10 separate to open the external vestibule.

329   Our *in vitro* assays showed that while DraNramp metal transport requires sampling of both

330   outward- and inward-open states, proton uniport occurs in sterically outward-locked constructs.

331   This supports a model where protons and metal travel through distinct pathways on the

332   cytoplasmic side of the protein (Figure 7C-D), such that proton uniport is a feature of DraNramp's

333   outward-open state, whereas metal transport requires bulk rearrangement. In contrast, both protons

334   and metal likely enter through the same aqueous pathway, as inward-locked proteins do not

335   transport either substrate. Proton uniport occurs via a network of conserved protonatable residues

336   leading from D56 in the metal-binding site to D131 in a salt-bridge network between TMs 3, 4, 8,

337   and 9. This proton pathway is accessible in the outward-open state, thus enabling the well-

338   documented proton uniport (Chen et al., 1999; Gunshin et al., 1997; Mackenzie et al., 2006; Nelson

339   et al., 2002; Xu et al., 2004). The predicted protonation of D56 and subsequent transfer to D131,

340   mediated through an E134/H232-stabilized transition state, may thus serve to restrain H^+ entry.

341   For metal-proton co-transport, Mn^{2+} interaction with D56 presumably stimulates proton transfer

342   into the same salt-bridge network. We further explore the mechanistic details of DraNramp

343   "proton-metal coupling" in an accompanying paper (Bozzi et al., 2018).

16

344   In our G223W structure, two water molecules coordinate Mn^{2+}: one lies between the metal and

345   A227's carbonyl, the other the metal and Q378 **(**Figures 4A and 7E). We propose that after Mn^{2+}

346   binds to D56, M230, A53, and N59 as in our G223W structure, the A227 carbonyl and Q378 both

347   displace the two waters as the outer gate closes. DraNramp would thus reach a fully dehydrated

348   metal-bound state not yet visualized but which may resemble our apo G45R inward-occluded

349   structure (Figure 7E). Next, as the inner gate opens, the A53 carbonyl would exchange with a

350   nearby water—such as the one bound to H232 in our G223W structure—as would Q378, to yield

351   an inward-open metal-bound state as observed in the ScaNramp structure (Figures 4B and 7E)

352   (Ehrnstorfer et al., 2014). In this conformation the Mn^{2+}-coordination sphere would include four

353   residues and two waters—analogous to the G223W structure—thus facilitating eventual metal

354   release. The proposed transition from four to six to four Mn^{2+}-coordinating residues could help

355   preferentially stabilize the occluded transition state(Shilton, 2015) through the free energy

356   (entropy-driven) gains of releasing the two water ligands. Furthermore, the rearrangements needed

357   to achieve the hypothetical intermediate six-residue Mn^{2+} coordination—the helical extension and

358   inward movement of TM6a, and the toppling of TM10's top half—also close the external

359   vestibule, providing a potential mechanistic link between local metal-coordination changes and

360   bulk conformational change. To return to the outward-open state, the transporter must pass through

361   an apo-occluded state as seen in the G45R structure, in which the N59 and Q378 sidechains

362   reorient to stabilize D56 in the absence of the divalent cation carried during the outward-to-inward

363   transition (Figures 4C and 7E). As the transporter reaches the outward-open state seen in

364   EcoNramp (Ehrnstorfer et al., 2017) and our apo G223W structure, a protonation event at D56

365   may prime the binding site to receive another incoming metal ion. Future molecular dynamic

366   simulations and/or experiments will be essential to test these predictions.

367   The mechanism described above for the DraNramp transport cycle—developed from structures of

368   the same Nramp homolog in three distinct conformations and supported by metal and proton

369   transport data—differs significantly from those previously observed for other LeuT-fold

370   transporters. Mhp1, BetP, and (to a lesser degree) LeuT generally obey a "rocking bundle" model

371   in which the rigid-body movement of four TMs that contain the primary substrate binding site (1,

372   2, 6, and 7) against the remaining TMs (3-5, 8-10) leads to conformational change (Forrest and

373   Rudnick, 2009; Kazmier et al., 2017; Shi, 2013). In DraNramp TMs 4, 5, and 10 join TMs 1 and

374   6 to form the substrate-binding "mobile domain," while TMs 2 and 7 join the remaining TMs as

375   part of the scaffold. Furthermore, the mobile helices do not move as rigid bodies, as conserved

376   helix-breaking motifs free TMs 1a, 6a, and the top of TM10 to move independent of TMs 1b, 6b

377   and the bottom of TM10. In contrast, the fully-helical TM5 wholly reorients, and may thus

378   coordinate the opening and closing of the inner and outer gates, connecting TMs 1a, 4, and 6b with

379   TM6a (Figures 2 and 7A-B).

380   In comparison to other APC superfamily members, the large TM1a displacement in DraNramp

381   most closely resembles its dramatic movement in LeuT(Krishnamurthy and Gouaux, 2012). Gating

382   roles for TMs 5 and 10 have been ascribed for BetP, Mhp1, and MhsT (Malinauskaite et al., 2014;

383   Ressl et al., 2009; Shimamura et al., 2010), although not as extensive as we propose here in

384   DraNramp. Not surprisingly, the DraNramp conformational changes are most similar to those

385   predicted by comparing structures of two other bacterial Nramp homologs in complementary

386   conformations (Ehrnstorfer et al., 2014; Ehrnstorfer et al., 2017), suggesting conservation within

387   the Nramp clade of the LeuT-fold family.

388   Whereas the distinct conformational changes of DraNramp demonstrate the diverse repertoire of

389   dynamics available to the LeuT-fold family, the most striking mechanistic differences between

18

390   DraNramp and other structurally-studied LeuT-fold transporters concern the coupling ion

391   behavior. Most well-characterized members (including LeuT, BetP, and Mhp1) are Na^+-driven

392   symporters of small organic molecules which have one or two Na^+-binding sites (Perez and

393   Ziegler, 2013; Rudnick, 2013). Sodium binding at the highly-conserved Na2 site connects the

394   "bundle" (TM1) and "scaffold" (TM8) domains while also shifting the conformational equilibrium

395   to favor the outward-open state (Claxton et al., 2010; Tavoulari et al., 2016; Zhao et al., 2011).

396   This Na2 site consists of hydroxyls from two consecutive serines/threonines on TM8 and four

397   main-chain carbonyls (one from TM8, three from the unwound-region of TM1) (Perez and Ziegler,

398   2013; Yamashita et al., 2005). Intriguingly, the analogous location in DraNramp also contains

399   highly-conserved hydroxyl-providing TM8 residues S327 (92%) and S328 (20%, 74% T), which

400   may be remnants of the ancestral Na2 site conversion into a H^+ site in the Nramp clade. This

401   hypothetical evolutionary switch has precedent within the LeuT-fold family, as the proton-coupled

402   amino acid transporter ApcT analogously uses a conserved TM5 lysine (K158), whose sidechain

403   protrudes into the Na2 location, as its primary proton-binding site (Shaffer et al., 2009). The

404   sodium-to-proton switch may have evolved in Nramps to avoid simultaneously coordinating two

405   metal cations (Na^+ coordination, like Mn^{2+} coordination, requires ~6 oriented ligands, whereas H^+

406   binding requires a single sidechain).

407   LeuT and other bacterial homologs also antiport a proton as they return to an outward-open state

408   (Kantcheva et al., 2013; Zhao et al., 2010; Zomot et al., 2007) via a conserved glutamate (E290)

409   on TM7 (Malinauskaite et al., 2016), analogous to the highly-conserved N275 (100%) that lines

410   DraNramp's intracellular vestibule. Available structures and MD simulations suggest that proton

411   symport in ApcT and antiport in LeuT likely occur through the bulk opening and closing of the

412   same permeation pathways used by the primary substrates (amino acids) (Krishnamurthy and

19

413   Gouaux, 2012; Malinauskaite et al., 2016; Shaffer et al., 2009; Shi and Weinstein, 2010). In

414   contrast DraNramp does H^+ uniport even when mutationally (G223W) or chemically (A61C-

415   MTSET) precluded from opening the intracellular vestibule (Figure 5). We propose a proton route

416   from D56 through D131 and into a conserved salt-bridge network between TMs 3, 4, 8, and 9

417   (Figure 6), which remain relatively stationary during the conformational change process (Figure

418   2). Indeed, evolutionary analysis reveals that this polar network is unique to the Nramp clade of

419   the LeuT-family (Cellier, 2016); this region is mainly hydrophobic in both LeuT and ApcT

420   (Shaffer et al., 2009; Yamashita et al., 2005). A parallel transport pathway for protons alleviates

421   the electrostatic problem of stabilizing three added positive charges (the proton and divalent metal

422   cation) throughout the conformational change process. Such proton uniport requiring only subtle

423   conformational rearrangements is more reminiscent of H^+ shuttling in the CLC family of Cl^-/H^+

424   antiporters (Accardi and Miller, 2004; Accardi and Picollo, 2010; Basilio et al., 2014; Miller, 2006)

425   than the canonical Na^+ transport seen in LeuT-family symporters.

426   The DraNramp proton and metal transport mechanism, where primary and driving substrates enter

427   via a common permeation pathway but exit via separate routes to the cytoplasm—with H^+ transfer

428   perhaps preceding and triggering bulk conformational rearrangement needed for Mn^{2+} release to

429   occur—is thus far unique to the Nramp clade within the APC superfamily. This new model for

430   Nramp transport therefore illustrates the evolutionary flexibility and adaptability of the shared

431   LeuT fold.

432

433   **Methods**

434   *Cloning of DraNramp*

435   WT and mutant DraNramps were cloned in pET21-N8H as described (Bozzi et al., 2016b). All

436   constructs were full-length, except the G223W crystallization construct was N-terminally

437   truncated to residue 35; this deletion did not affect metal transport (Bozzi et al., 2016b). Mutations

438   were made using the Quikchange mutagenesis protocol (Stratagene) and confirmed by DNA

439   sequencing. Single-cysteine constructs also included the C382S mutation to remove the lone

440   endogenous cysteine. The C41(DE3) *E. coli* strain was used for protein expression and *in vivo*

441   assays.

442

443   *Expression and purification of DraNramp crystallography constructs*

444   Six liters of DraNramp C41(DE3) cells were cultured as described (Bozzi et al., 2016b), pelleted

445   and flash-frozen in liquid nitrogen. Proteins were purified at 4°C. Thawed cells were lysed by

446   sonication in 40 ml load buffer (20 mM sodium phosphate, pH 7.5, 55 mM imidazole, 500 mM

447   NaCl, 10% (v/v) glycerol) plus 1 mM PMSF, 1 mM benzamidine, and 0.3 mg/ml each DNAse I

448   and lysozyme. Lysates were cleared for 20 min at $27,000 \times g$. Membranes were pelleted from

449   supernatant at $230,000 \times g$ for 70 min, homogenized in 65 ml load buffer and flash-frozen in liquid

450   nitrogen. Thawed membranes were solubilized for 1 h, adding 1.5% (w/v) n-dodecyl-β-D-

451   maltopyranoside (DDM), then spun at $140,000 \times g$ for 35 min to pellet debris. Pre-equilibrated Ni-

452   sepharose beads (3 mL; GE Healthcare) were incubated with the supernatant for 1 h, and washed

453   with load buffer containing sequentially 0.03 % DDM, 0.5% lauryl maltose neopentyl glycol

454   (LMNG), and 0.1% LMNG. Protein was eluted in 20 mM sodium phosphate, pH 7.5, 450 mM

455   imidazole, 500 mM NaCl, 10% (v/v) glycerol, 0.01% LMNG, concentrated to < 0.5 mL in a 50-

456   kDa cutoff centrifugal concentrator, and loaded onto a Superdex S200 10/300 (GE Healthcare)

457   pre-equilibrated with SEC buffer (10 mM HEPES pH 7.5, 150 mM NaCl, 0.003% LMNG). Peak

458   fractions were pooled, concentrated to ~20-40 mg/ml, aliquoted, and flash-frozen in liquid

459   nitrogen.

460

461   *DraNramp crystallization, X-ray diffraction data collection, and structure determination*

462   Protein (10-15 μL) was loaded into a 100-μL glass syringe attached to an LCP coupling device

463   (Formulatrix). A second 100-μL syringe containing 1.5 volumes of liquid monoolein (T > 37°C)

464   was attached to the coupling device, and the two solutions were mixed for 100 cycles using an

465   NT8 (Formulatrix) in LCP mixing mode at 5 mm/s. LCP boluses (50-100 nL) and precipitant (600-

466   1000 μL) were dispensed into 96-well LCP glass plates and incubated at room temperature (RT).

467   Crystals of G223W (25 mg/ml) with 2.5 mM $MnCl_2$ in SEC buffer grown in 28% PEG400, 5 mM

468    $MnCl_2$, 100 mM MES pH 6, 50 mM succinic acid pH 6, 10 mM spermidine pH 7, (10-30 μm

469   square plates) were harvested after nine days using mesh loops (MiTeGen) to scoop the bolus, then

470   flash-frozen in liquid nitrogen. Similar G223W crystals in the apo state were obtained after seven

471   days with 26% PEG400, 100 mM MES pH 6, 50 mM succinic acid pH 6, 20 mM spermidine pH

472   7. Crystals of the analogous NEM-modified G223C/C382S ΔN34 (G223C retains close to WT-

473   level metal transport before NEM-labeling (Bozzi et al., 2016b)) were obtained in the same

474   condition. Crystals of G45R (22 mg/ml) grown in 20% PEGMME 550, 150 mM NaCl, 100 mM

475   HEPES, pH 7.0 (~100 μm rods) were harvested after ~10 days.

476   Data were collected at Advanced Photon Source beamline 24ID-C. Crystals were located by grid

477   scanning with a 70-μm beam at 70% transmission followed by focused grid scanning with a 10-

478   μm beam at 100% transmission. Data wedges were typically collected from -30° to +30° in 0.2°

479   increments using a 10-μm beam at 100% transmission. Two wedges from 2 crystals (G45R), 23

480   wedges from ~15 crystals (G223W with Mn^{2+}), or 39 wedges from ~20 crystals (G223W apo)

481 were independently indexed and integrated then combined during scaling using HKL2000

482 (Otwinowski and Minor, 1997) to obtain complete datasets. Structures were determined using

483 software provided by SBgrid (Morin et al., 2013). Initial phases were obtained by molecular

484 replacement in PHASER (McCoy et al., 2007) using our first DraNramp structure (PDB: 5KTE)

485 as a search model for G45R and an in-progress G45R model for G223W. Model building and

486 refinement were iterated in Coot(Emsley and Cowtan, 2004) and PHENIX (Adams et al., 2010),

487 respectively. For all structures, positional and B-factor refinement with TLS restraints were used

488 throughout, with torsion angle and NCS restraints for G45R, and secondary structure restraints for

489 the Patch mutant. G45R contains two protein molecules in the asymmetric unit—chain A with

490 residues 45-167 and 174-436 and chain B with residues 44-168 and 175-436 (RMSD 0.86 Å over

491 2899 atoms, 0.50 Å over all 386 Cαs)—and seven fully or partly modeled monoolein molecules.

492 Chain A was used for figures and analyses. The G223W Mn^{2+}-bound structure includes residues

493 39-436, nine full or partial monooleins, one spermidine molecule, and two Mn^{2+} ions—one in the

494 metal-binding site, one at a crystal-packing interface. The G223W apo structure includes residues

495 39-436 and six full or partial monooleins. The two G223W structures align with RMSD 1.41 Å

496 over 3012 atoms, 1.08 Å over all 398 Cαs). The electron density for each TM is shown in Figure

497 Figure 2—figure supplement 2A for G45R and Figure 2—figure supplement 2B for G223W with

498 Mn^{2+}, while Figure 2—figure supplement 2C shows the metal-binding site for both the Mn^{2+}-

499 bound and apo G223W structures. The inward-open Patch mutant structure was updated to correct

500 the position of intracellular loop 10-11 and the registry of TM11, and extend the N-termini of TMs

501 5, 7 and 9, the C-terminus of TM7, and extracellular loop 7-8, and improve the geometry of the

502 Fab. The new model comprises residues 43-165, 170-236, 256-341, 351-436 of DraNramp, 1-129

503 and 132-213, and 1-213 of the Fab heavy and light chains, respectively, and three Os^{3+} ions.

504

505   *In vivo metal transport assays*

506   Metal uptake assays in *E. coli* were performed as described previously (Bozzi et al., 2016a). For

507   each biological replicate reported in figure legends, a separate culture of transformed *E. coli* was

508   grown and induced to express the exogenous Nramp construct.

509

510   *In vitro transport assays*

511   Protein purification, liposome preparation, and metal/proton transport assays were performed as

512   described in an accompanying paper (Bozzi et al., 2018). Single-cysteine constructs A53C and

513   A61C were purified in the presence of 1 mM DTT. To modify cysteines, liposomes were diluted

514   into buffer (120 mM NaCl, 10 mM MOPS pH 7) containing 3 mM MTSET, 3 mM MTSEA, or 4

515   mM NEM, and incubated at least 30 min at RT before beginning transport assays. For each

516   technical replicate reported in figure legends, a separate aliquot of dye-loaded proteoliposomes

517   was diluted into the appropriate outside buffer, including cysteine modifiers if applicable, then

518   fluorescence time course data were collected before and after addition of valinomycin, metal

519   substrate, and/or ionomycin.

520

521   *Cysteine accessibility measurements*

522   Cells grown as for the uptake assay were washed once in labeling buffer, resuspended at $OD_{600}=2$,

523   and aliquoted 100 μL per well in a 96-well plate. A 1:1 NEM dilution series was prepared in

524   labeling buffer at 8 mM; 100 μL of the appropriate 2X NEM solution was added to each well and

525   incubated 15 min at RT. L-cysteine (10 μL of 200 mM) was added to quench NEM. Cells were

526   washed twice in labeling buffer, pelleted, resuspended in 30 μL lysis and denaturing buffer (6 M

24

527   urea, 0.1% SDS, 100 mM Tris pH 7) with 0.5 mM DTT and incubated 1 h at 37°C. The lysate (10

528   μL) was mixed with 3.5 μL of 6 mM 5K-PEG maleimide (Creative PEGWORKS) in lysis and

529   denaturing buffer, incubated 1 h at 37°C, and the reaction terminated by adding sample buffer with

530   β-mercaptoethanol. Protein was detected via SDS-PAGE and Western blotting using an Alexa

531   647-conjugated anti-His-tag antibody (QIAGEN) and a Typhoon Imager (GE Healthcare).

532   ImageJ64 was used to determine the % modification as described (Bozzi et al., 2016b). For each

533   biological replicate reported in figure legends, a separate culture of transformed *E. coli* was grown

534   and induced to express the exogenous Nramp construct.

535

536   *Sequence alignments*

537   An alignment of 9289 Nramp sequences was obtained from a HMMER (Finn et al., 2011) search

538   using the DraNramp sequence with an E-value of 1, filtered for sequences with just one domain,

539   then filtered for sequences 400-600 residue long. Incomplete sequences and sequences lacking the

540   canonical Nramp TM1 "DPGN" and TM6 "MPH" motifs were removed, yielding 6878 sequences.

541   A seed of 92 diverse sequences were aligned using MUSCLE (Edgar, 2004), then HMMER was

542   used with a gap threshold of 0.99 to create the final alignment (Figure 2—source data 1).

543

544   *Structural comparisons and analyses*

545   Per-residue Cα RMSD values were calculated using the ColorByRMSD PyMOL script, and

546   whole-structure Cα RMSD values using the PyMOL align command with cycles=0. To generate

547   the distance difference matrices, the pairwise distances between all Cα atoms were calculated for

548   each structure (inward, inward-occluded, and outward). Then, for each combination of two

549   conformations, a distance difference matrix was calculated by taking the difference between the

25

550 distance matrices corresponding to each conformation. These distance-difference values were then

551 averaged for each pair of TM helices (after dividing TMs 1, 6, and 10 into "a" and "b" segments)

552 using an RMSD-like calculation to obtain a 14✕14 matrix for each pair of conformations. pK_a

553 values were calculated using PROPKA (Dolinsky et al., 2004) with CHARMM forcefields.

554

Data availability

556 The accession number for the DraNramp crystal structures reported in this paper are G45R inward-

557 occluded, PDB ID: 6C3I; G223W ΔN34 outward-open with Mn^{2+}, PDB ID: 6BU5; G223W ΔN34

558 outward-open apo, PDB ID: 6D91; revised inward open, PDB ID: 6D9W. The unprocessed

559 diffraction images were deposited in the Structural Biology Data Grid (https://data.sbgrid.org/)

560 with SBDG ID: 567 (G45R); 564 and 576 (G223W ΔN34 Mn^{2+}-bound and apo respectively); and

561 332, 333, and 334 (inward-open). The raw biochemical data that support the findings of this study

562 are available from the corresponding author upon reasonable request.

563

Author Contributions

565 R.G. oversaw and designed the research with A.T.B. and C.M.Z.; A.T.B. performed all functional

566 assays and analyzed the resulting data; B.K.L. designed, cloned, and initially validated the panel

567 of tryptophan mutants with A.T.B.; C.M.Z, obtained crystals and diffraction data and solved the

568 structure of G45R DraNramp; A.T.B. obtained crystals and diffraction data and solved the

569 structures of G223W ΔN34 DraNramp, with assistance at each stage from J.M.N., C.M.Z., and/or

570 R.G.; R.G. corrected the registry and re-refined the original DraNramp structure; C.H.Z.

571 computationally analyzed Nramp sequences and structures. A.T.B., C.M.Z., and R.G. wrote the

572 manuscript, with input from all authors.

26

573

Competing Interests

575   The authors declare no competing interests.

576

585

References

587   Accardi, A., and Miller, C. (2004). Secondary active transport mediated by a prokaryotic
588   homologue of ClC Cl- channels. Nature *427*, 803-807.

589   Accardi, A., and Picollo, A. (2010). CLC channels and transporters: Proteins with borderline
590   personalities. Biochimica Et Biophysica Acta-Biomembranes *1798*, 1457-1464.

591   Adams, P.D., Afonine, P.V., Bunkoczi, G., Chen, V.B., Davis, I.W., Echols, N., Headd, J.J., Hung,
592   L.-W., Kapral, G.J., Grosse-Kunstleve, R.W.*, et al.* (2010). PHENIX: a comprehensive Python-
593   based system for macromolecular structure solution. Acta Crystallographica Section D-
594   Biological Crystallography *66*, 213-221.

595   Barber-Zucker, S., Shaanan, B., and Zarivach, R. (2017). Transition metal binding selectivity
596   in proteins and its correlation with the phylogenomic classification of the cation diffusion
597   facilitator protein family. Scientific Reports *7*.

598   Barrios, M., Moreno-Carralero, M.-I., Cuadrado-Grande, N., Baro, M., Vivanco, J.-L., and
599   Moran-Jimenez, M.-J. (2012). The homozygous mutation G75R in the human SLC11A2 gene
600   leads to microcytic anaemia and iron overload. British Journal of Haematology *157*, 514-
601   516.

602   Basilio, D., Noack, K., Picollo, A., and Accardi, A. (2014). Conformational changes required
603   for H+/Cl- exchange mediated by a CLC transporter. Nature Structural & Molecular Biology
604   *21*, 456-463.

605   Boudker, O., and Verdon, G. (2010). Structural perspectives on secondary active
606   transporters. Trends in Pharmacological Sciences *31*, 418-426.

607   Bozzi, A.T., Bane, L.B., Weihofen, W.A., McCabe, A.L., Singharoy, A., Chipot, C.J., Schulten, K.,
608   and Gaudet, R. (2016a). Conserved methionine dictates substrate preference in Nramp-
609   family divalent metal transporters. Proceedings of the National Academy of Sciences of the
610   United States of America *113*, 10310-10315.

611   Bozzi, A.T., Bane, L.B., Weihofen, W.A., Singharoy, A., Guillen, E.R., Ploegh, H.L., Schulten, K.,
612   and Gaudet, R. (2016b). Crystal Structure and Conformational Change Mechanism of a
613   Bacterial Nramp-Family Divalent Metal Transporter. Structure *24*, 2102-2114.

614   Bozzi, A.T., Bane, L.B., Zimanyi, C.M., and Gaudet, R. (2018). Proton co-transport and voltage
615   dependence enforce unidirectional metal transport in an Nramp transporter.

616   Cellier, M.F.M. (2012). Nramp: from Sequence to Structure and Mechanism of Divalent
617   Metal Import. Metal Transporters *69*, 249-293.

618   Cellier, M.F.M. (2016). Evolutionary analysis of Slcll mechanism of proton-coupled metal-
619   ion transmembrane import. Aims Biophysics *3*, 286-318.

620   Chen, X.Z., Peng, J.B., Cohen, A., Nelson, H., Nelson, N., and Hediger, M.A. (1999). Yeast SMF1
621   mediates H+-coupled iron uptake with concomitant uncoupled cation currents. Journal of
622   Biological Chemistry *274*, 35089-35094.

623   Claxton, D.P., Quick, M., Shi, L., de Carvalho, F.D., Weinstein, H., Javitch, J.A., and McHaourab,
624   H.S. (2010). Ion/substrate-dependent conformational dynamics of a bacterial homolog of
625   neurotransmitter: sodium symporters. Nature Structural & Molecular Biology *17*, 822-
626   U868.

627   Courville, P., Chaloupka, R., and Cellier, M.F.M. (2006). Recent progress in structure-
628   function analyses of Nramp proton-dependent metal-ion transporters. Biochemistry and
629   Cell Biology-Biochimie Et Biologie Cellulaire *84*, 960-978.

630   Dolinsky, T.J., Nielsen, J.E., McCammon, J.A., and Baker, N.A. (2004). PDB2PQR: an
631   automated pipeline for the setup of Poisson-Boltzmann electrostatics calculations. Nucleic
632   Acids Research *32*, W665-W667.

633   Edgar, R.C. (2004). MUSCLE: multiple sequence alignment with high accuracy and high
634   throughput. Nucleic Acids Research *32*, 1792-1797.

635   Ehrnstorfer, I.A., Geertsma, E.R., Pardon, E., Steyaert, J., and Dutzler, R. (2014). Crystal
636   structure of a SLC11 (NRAMP) transporter reveals the basis for transition-metal ion
637   transport. Nature Structural & Molecular Biology *21*, 990-996.

638   Ehrnstorfer, I.A., Manatschal, C., Arnold, F.M., Laederach, J., and Dutzler, R. (2017).
639   Structural and mechanistic basis of proton-coupled metal ion transport in the
640   SLC11/NRAMP family. Nature Communications *8*.

641   Emsley, P., and Cowtan, K. (2004). Coot: model-building tools for molecular graphics. Acta
642   Crystallographica Section D-Biological Crystallography *60*, 2126-2132.

643   Finn, R.D., Clements, J., and Eddy, S.R. (2011). HMMER web server: interactive sequence
644   similarity searching. Nucleic Acids Research *39*, W29-W37.

645   Forrest, L.R., Kramer, R., and Ziegler, C. (2011). The structural basis of secondary active
646   transport mechanisms. Biochimica Et Biophysica Acta-Bioenergetics *1807*, 167-188.

647   Forrest, L.R., and Rudnick, G. (2009). The Rocking Bundle: A Mechanism for Ion-Coupled
648   Solute Flux by Symmetrical Transporters. Physiology *24*, 377-386.

649   Glasfeld, A., Guedon, E., Helmann, J.D., and Brennan, R.G. (2003). Structure of the
650   manganese-bound manganese transport regulator of Bacillus subtilis. Nature Structural
651   Biology *10*, 652-657.

652   Gunshin, H., Mackenzie, B., Berger, U.V., Gunshin, Y., Romero, M.F., Boron, W.F., Nussberger,
653   S., Gollan, J.L., and Hediger, M.A. (1997). Cloning and characterization of a mammalian
654   proton-coupled metal-ion transporter. Nature *388*, 482-488.

655   Kantcheva, A.K., Quick, M., Shi, L., Winther, A.M.L., Stolzenberg, S., Weinstein, H., Javitch, J.A.,
656   and Nissen, P. (2013). Chloride binding site of neurotransmitter sodium symporters.
657   Proceedings of the National Academy of Sciences of the United States of America *110*, 8489-
658   8494.

659   Kazmier, K., Claxton, D.P., and McHaourab, H.S. (2017). Alternating access mechanisms of
660   LeuT-fold transporters: trailblazing towards the promised energy landscapes. Current
661   Opinion in Structural Biology *45*, 100-108.

662   Kazmier, K., Sharma, S., Islam, S.M., Roux, B., and McHaourab, H.S. (2014a). Conformational
663   cycle and ion-coupling mechanism of the Na+/hydantoin transporter Mhp1. Proceedings of
664   the National Academy of Sciences of the United States of America *111*, 14752-14757.

665   Kazmier, K., Sharma, S., Quick, M., Islam, S.M., Roux, B., and Weinstein, H. (2014b).
666   Conformational dynamics of ligand-dependent alternating access in LeuT. *21*, 472-479.

667   Krishnamurthy, H., and Gouaux, E. (2012). X-ray structures of LeuT in substrate-free
668   outward-open and apo inward-open states. Nature *481*, 469-U480.

669   Kumar, H., Kasho, V., Smirnova, I., Finer-Moore, J.S., Kaback, H.R., and Stroud, R.M. (2014).
670   Structure of sugar-bound LacY. Proc Natl Acad Sci U S A *111*, 1784-1788.

671   Ma, D., Lu, P.L., Yan, C.Y., Fan, C., Yin, P., Wang, J.W., and Shi, Y.G. (2012). Structure and
672   mechanism of a glutamate-GABA antiporter. Nature *483*, 632-U161.

673   Mackenzie, B., Ujwal, M.L., Chang, M.H., Romero, M.F., and Hediger, M.A. (2006). Divalent
674   metal-ion transporter DMT1 mediates both H+-coupled Fe2+ transport and uncoupled
675   fluxes. Pflugers Archiv-European Journal of Physiology *451*, 544-558.

676   Malinauskaite, L., Quick, M., Reinhard, L., Lyons, J.A., Yano, H., Javitch, J.A., and Nissen, P.
677   (2014). A mechanism for intracellular release of Na+ by neurotransmitter/sodium
678   symporters. Nature Structural & Molecular Biology *21*, 1006-1012.

679   Malinauskaite, L., Said, S., Sahin, C., Grouleff, J., Shahsavar, A., Bjerregaard, H., Noer, P.,
680   Severinsen, K., Boesen, T., Schiott, B.*, et al.* (2016). A conserved leucine occupies the empty
681   substrate site of LeuT in the Na+-free return state. Nature Communications *7*.

682   McCoy, A.J., Grosse-Kunstleve, R.W., Adams, P.D., Winn, M.D., Storoni, L.C., and Read, R.J.
683   (2007). Phaser crystallographic software. Journal of Applied Crystallography *40*, 658-674.

684   Miller, C. (2006). CIC chloride channels viewed through a transporter lens. Nature *440*, 484-
685   489.

686   Morin, A., Eisenbraun, B., Key, J., Sanschagrin, P.C., Timony, M.A., Ottaviano, M., and Sliz, P.
687   (2013). Collaboration gets the most out of software. Elife *2*.

688   Nelson, N., Sacher, A., and Nelson, H. (2002). The significance of molecular slips in transport
689   systems. Nature Reviews Molecular Cell Biology *3*, 876-881.

690   Nevo, Y., and Nelson, N. (2006). The NRAMP family of metal-ion transporters. Biochimica Et
691   Biophysica Acta-Molecular Cell Research *1763*, 609-620.

692   Otwinowski, Z., and Minor, W. (1997). Processing of X-ray diffraction data collected in
693   oscillation mode. Macromolecular Crystallography, Pt A *276*, 307-326.

694   Perez, C., and Ziegler, C. (2013). Mechanistic aspects of sodium-binding sites in LeuT-like
695   fold symporters. Biol Chem *394*, 641-648.

696   Perland, E., and Fredriksson, R. (2017). Classification Systems of Secondary Active
697   Transporters. Trends in Pharmacological Sciences *38*, 305-315.

698   Pujol-Gimenez, J., Hediger, M.A., and Gyimesi, G. (2017). A novel proton transfer mechanism
699   in the SLC11 family of divalent metal ion transporters. Scientific Reports *7*.

700   Ressl, S., van Scheltinga, A.C.T., Vonrhein, C., Ott, V., and Ziegler, C. (2009). Molecular basis
701   of transport and regulation in the Na+/betaine symporter BetP. Nature *458*, 47-U41.

702   Richards, F.M., and Kundrot, C.E. (1988). Identification of Structural Motifs from Protein
703   Coordinate Data - Secondary Structure and 1st-Level Supersecondary Structure. Proteins-
704   Structure Function and Genetics *3*, 71-84.

705   Rudnick, G. (2013). How do transporters couple solute movements? Molecular Membrane
706   Biology *30*, 355-359.

707   Shaffer, P.L., Goehring, A., Shankaranarayanan, A., and Gouaux, E. (2009). Structure and
708   Mechanism of a Na+-Independent Amino Acid Transporter. Science *325*, 1010-1014.

709   Shi, L., and Weinstein, H. (2010). Conformational Rearrangements to the Intracellular Open
710   States of the LeuT and ApcT Transporters Are Modulated by Common Mechanisms.
711   Biophysical Journal *99*, L103-L105.

712   Shi, Y. (2013). Common Folds and Transport Mechanisms of Secondary Active
713   Transporters. Annual Review of Biophysics, Vol 42 *42*, 51-72.

714   Shilton, B.H. (2015). Active transporters as enzymes: an energetic framework applied to
715   major facilitator superfamily and ABC importer systems. Biochemical Journal *467*, 193-199.

716   Shimamura, T., Weyand, S., Beckstein, O., Rutherford, N.G., Hadden, J.M., Sharples, D.,
717   Sansom, M.S.P., Iwata, S., Henderson, P.J.F., and Cameron, A.D. (2010). Molecular Basis of
718   Alternating Access Membrane Transport by the Sodium-Hydantoin Transporter Mhp1.
719   Science *328*, 470-473.

720   Smirnova, I., Kasho, V., Sugihara, J., and Kaback, H.R. (2013). Trp replacements for tightly
721   interacting Gly-Gly pairs in LacY stabilize an outward-facing conformation. Proceedings of
722   the National Academy of Sciences of the United States of America *110*, 8876-8881.

723   Tavoulari, S., Margheritis, E., Nagarajan, A., DeWitt, D.C., Zhang, Y.-W., Rosado, E., Ravera, S.,
724   Rhoades, E., Forrest, L.R., and Rudnick, G. (2016). Two Na+ Sites Control Conformational
725   Change in a Neurotransmitter Transporter Homolog. Journal of Biological Chemistry *291*,
726   1456-1471.

727   Vastermark, A., Wollwage, S., Houle, M.E., Rio, R., and Saier, M.H. (2014). Expansion of the
728   APC superfamily of secondary carriers. Proteins-Structure Function and Bioinformatics *82*,
729   2797-2811.

730   Weyand, S., Shimamura, T., Yajima, S., Suzuki, S., Mirza, O., Krusong, K., Carpenter, E.P.,
731   Rutherford, N.G., Hadden, J.M., O'Reilly, J.*, et al.* (2008). Structure and Molecular Mechanism
732   of a Nucleobase-Cation-Symport-1 Family Transporter. Science *322*, 709-713.

733   Wong, F.H., Chen, J.S., Reddy, V., Day, J.L., Shlykov, M.A., Wakabayashi, S.T., and Saier, M.H.
734   (2012). The Amino Acid-Polyamine-Organocation Superfamily. J Mol Microbiol Biotechnol
735   *22*, 105-113.

736   Xu, H.X., Jin, J., DeFelice, L.J., Andrews, N.C., and Clapham, D.E. (2004). A spontaneous,
737   recurrent mutation in divalent metal transporter-1 exposes a calcium entry pathway. PLoS
738   biology *2*, 378-386.

739   Yamashita, A., Singh, S.K., Kawate, T., Jin, Y., and Gouaux, E. (2005). Crystal structure of a
740   bacterial homologue of Na+/Cl--dependent neurotransmitter transporters. Nature *437*,
741   215-223.

742   Zhao, Y., Terry, D.S., Shi, L., Quick, M., Weinstein, H., Blanchard, S.C., and Javitch, J.A. (2011).
743   Substrate-modulated gating dynamics in a Na+-coupled neurotransmitter transporter
744   homologue. Nature *474*, 109-U111.

745   Zhao, Y.F., Quick, M., Shi, L., Mehler, E.L., Weinstein, H., and Javitch, J.A. (2010). Substrate-
746   dependent proton antiport in neurotransmitter:sodium symporters. Nature Chemical
747   Biology *6*, 109-116.

748   Zomot, E., Bendahan, A., Quick, M., Zhao, Y.F., Javitch, J.A., and Kanner, B.I. (2007).
749   Mechanism of chloride interaction with neurotransmitter: sodium symporters. Nature *449*,
750   726-U729.
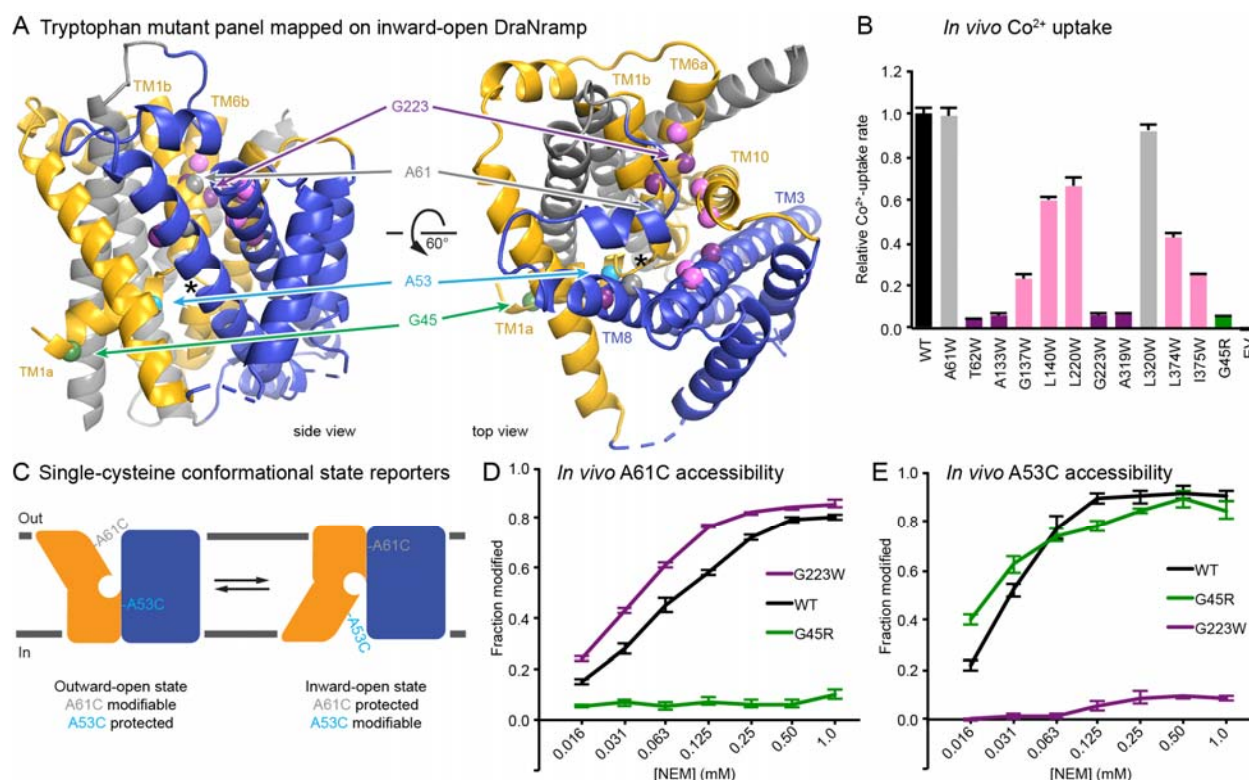
Figure 1. Design and validation of complementary conformationally-locked crystallization constructs.

(A) Panel of 11 designed tryptophan mutants (pink, purple, and gray spheres; see (B)) and G45R disease-mutant mimic (green) mapped onto our initial inward-facing DraNramp structure and color-coded by their effect on transport activity in (B). Single-cysteine reporters A53C (cyan) and A61C (gray) are indicated. TMs 1, 5, 6, and 10 are colored gold, TMs 3, 4, 8, and 9 blue, and TMs 2, 7, and 11 gray. * marks the approximate location of the metal-binding site. (B) Relative *in vivo* Co^{2+} uptake rates for tryptophan mutant panel. Mutants colored gray, pink and purple did not affect, moderately decreased, or eliminated uptake, respectively. (C) Two complementary single-cysteine reporters enable assessment of the mutants' conformational state preferences. For simplicity, in schematics DraNramp is depicted as two gold and blue domains that reorient to accomplish alternating access. (D) G45R prevented modification of the A61C outward-reporter, and (E) G223W fully protected the A53C inward-reporter, indicating that complementary conformational locking was achieved. Both reporters fully labeled the WT protein, likely because it cycles between both conformations during the assay. Data in B, D, and E are averages $\pm$ S.E.M. (n = 4). See also Figure 1—figure supplement 1.

33
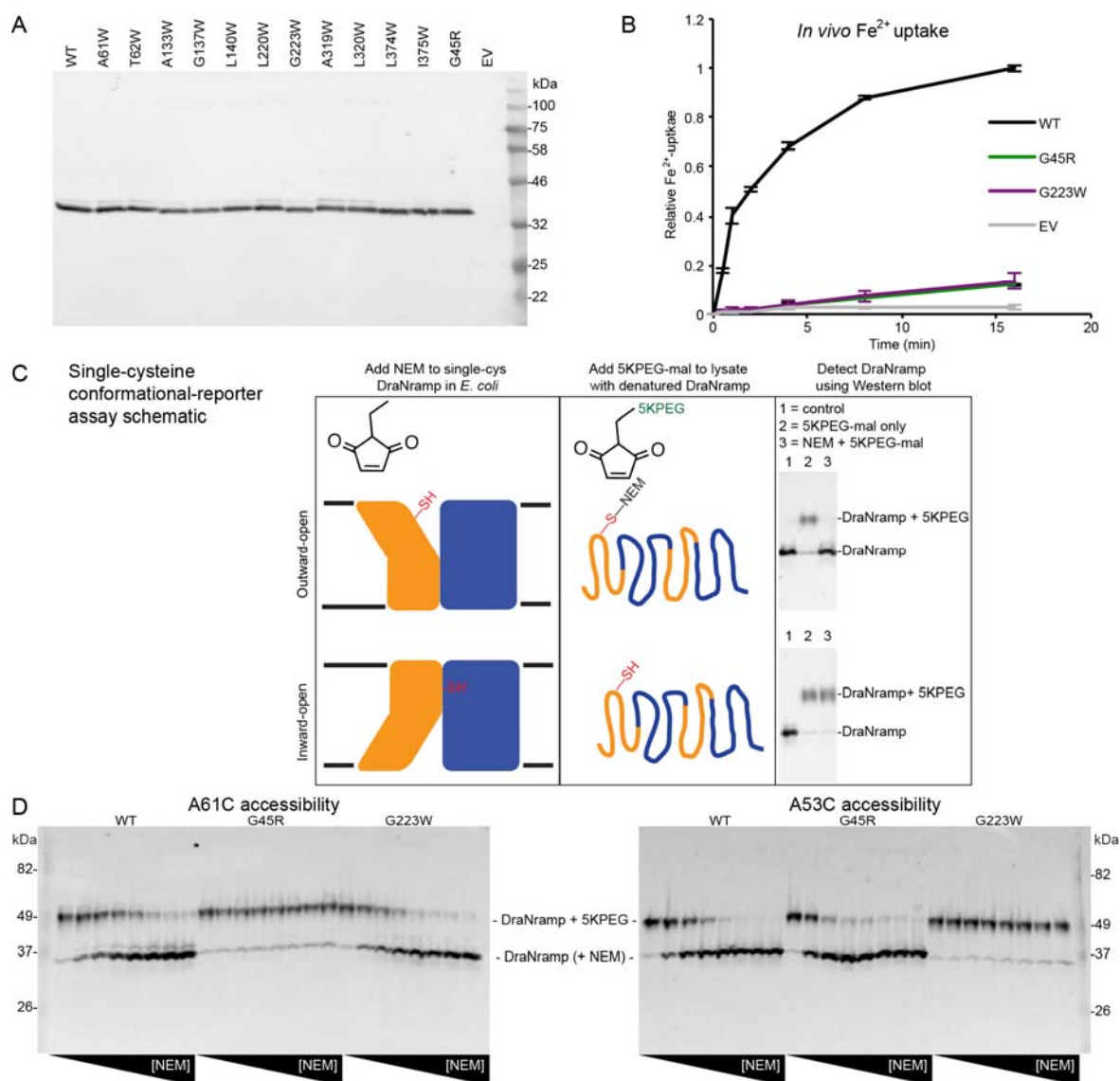
Figure 1—figure supplement 1. Validation of conformationally-locked crystallization constructs.

(A) Western blot against N-terminal His-tag for total lysates show most tryptophan mutants expressed similarly to WT DraNramp in *E. coli*. (B) Both G45R and G223W eliminated Fe^{2+} uptake in *E. coli*. (C) Schematic for cysteine accessibility assay two-step protocol using conformational reporters: first a gradient of NEM was applied to label any solvent-accessible cysteines, then the cells were lysed and protein denatured and 5K-PEG maleimide was added, which reacted with any previously unmodified cysteines. The 5K-PEG maleimide-labeled protein shifted upward from the NEM-labeled protein on SDS-PAGE. (D) G45R and G223W had opposing effects on single-cysteine reporter accessibility to NEM modification in *E. coli*. The A61C reporter—only solvent-exposed in the outward-facing state—was fully protected from NEM-labeling by the G45R mutation, indicating an inward-locked state. In contrast, A53C— likely only accessible in an inward-facing conformation—was fully protected from NEM-labeling by G223W, indicating an outward-locked state. Both reporters were fully labeled at high NEM concentrations for WT, suggesting the entire protein population cycles through both conformational states during the NEM labeling time.
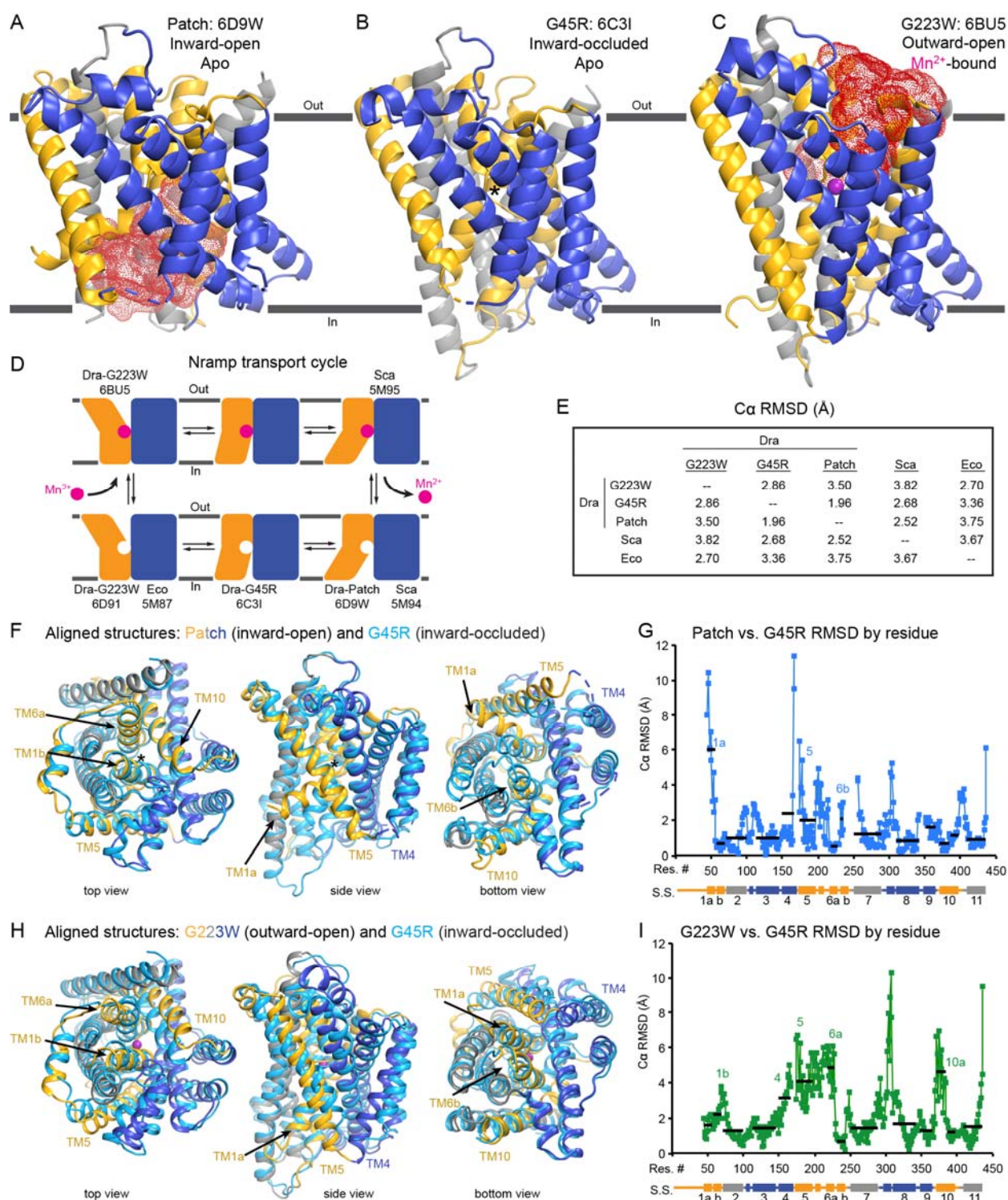
34

Table 1. DraNramp data collection and refinement statistics.

	Inward-open apo (Patch mutant + Fab)	Inward-occluded apo (G45R)	Outward-open Mn^{2+}-bound (G223W ΔN34)
PDB ID	6D9W	6C3I	6BU5
SBGrid Data Bank ID	332, 333, 334	567	564
Data Collection			
Wavelength (Å)	1.139	0.9793	0.9792
Resolution range (Å)	46.47 - 3.94 (4.08 - 3.94)	50.00-3.00 (3.05-3.00)	39.19-2.40 (2.49-2.40)
Space group	I222	$P2_12_12_1$	C121
Unit cell (a, b, c)	113.13, 132.08, 221.0	70.73, 97.85, 118.26	105.76, 80.39, 51.75
Unit cell (α, β, γ)	90.0, 90.0, 90.0	90.0, 90.0, 90.0	90.0, 94.72, 90.0
Number of crystals	3	2	~15
Total reflections	245867	66707	49321
Unique reflections	11791 (462)	17206 (842)	13983 (623)
Redundancy	16.6 (11.4)	3.9 (4.0)	3.5 (1.7)
Completeness (%)	95 (96)	98.5 (98.8)	82.1* (36.4)
Mean I/σ(I)	6 (.61)	6.41 (0.95)	6.25 (1.56)
R_{merge}	0.171	0.223 (1.388)	0.186
R_{meas}	0.177	0.270 (1.608)	0.210
R_{pim}	0.047	0.133 (0.795)	0.095
$CC_{1/2}$	0.99 (0.189)	0.993 (0.396)	0.984 (0.584)
Refinement			
Resolution range (Å)	46.47 - 3.94 (4.12 - 3.94)	30.0-3.0 (3.05-3.0)	39.19-2.40 (2.486-2.40)
R_{work}	0.271 (0.253)	0.249 (0.333)	0.238 (0.276)
R_{free}	0.309 (0.343)	0.270 (0.420)	0.272 (0.374)
Number of atoms	5764	5991	3213
Protein	5761	5812	3012
Ligand	3	150	139
Water	--	29	62
Protein residues	786	774	398
Ramachandran plot			
Favored (%)	754 (96.0)	760 (98.2)	389 (97.7)
Allowed (%)	32 (4.0)	14 (1.8)	9 (2.3)
Outliers (%)	0 (0.0)	0 (0.0)	0 (0.0)
RMS(bonds)	0.004	0.004	0.004
RMS(angles)	1.02	0.97	0.92
Average B-factor	90.3	61.38	72.6
Protein	90.3	61.40	72.1
Ligand	197.0	66.01	86.4
Water	--	32.82	63.8
Number of TLS groups	15	20	6

786   *The G223WdN34 dataset compiled from many small crystals is 99% complete to 3.4 Å, 95%
787   complete to 3.0 Å, 90% complete to 2.85 Å, 80% complete to 2.7 Å, and 60% complete to 2.5 Å.

35

Table 1—table supplement 1. Data collection and refinement statistics for apo G223W ΔN34.

|	**Outward-open Mn^{2+}-bound (G223W ΔN34)**
PDB ID	6D91
SBGrid Data Bank ID	576
Data Collection	
Wavelength (Å)	0.9792
Resolution range (Å)	38.14-2.356 (2.44-2.356)
Space group	C121
Unit cell (a, b, c)	101.92, 75.51, 53.15
Unit cell (α, β, γ)	90.0, 98.07, 90.0
Number of crystals	~20
Total reflections	48659 (367)
Unique reflections	10998 (256)
Redundancy	4.4 (1.4)
Completeness (%)	64.0* (15.6)
Mean I/σ(I)	8.83 (1.45)
R$_{merge}$	0.185
R$_{meas}$	0.203
R$_{pim}$	0.080
CC$_{1/2}$	0.986 (0.683)
Refinement	
Resolution range (Å)	39.19-2.356 (2.44-2.356)
R$_{work}$	0.244 (0.310)
R$_{free}$	0.295 (0.414)
Number of atoms	3100
Protein	3012
Ligand	71
Water	17
Protein residues	398
Ramachandran plot	
Favored (%)	380 (95.5)
Allowed (%)	17 (4.3)
Outliers (%)	1 (0.3)
RMS(bonds)	0.092
RMS(angles)	0.74
Average B-factor	56.6
Protein	56.5
Ligand	59.1
Water	80.3
Number of TLS groups	7

36

Figure 2. Crystal structures of DraNramp reveal two new conformations.
(A) Updated DraNramp Patch mutant structure in an inward-facing apo state with a wide intracellular aqueous vestibule (red mesh) (Bozzi et al., 2016b). TMs 1, 5, 6, and 10 are colored gold, TMs 3, 4, 8, and 9 blue, and TMs 2, 7, and 11 gray. (B) The G45R structure revealed an apo inward-occluded conformation with no substantial extracellular or intracellular aqueous pathway to the metal-binding site, denoted by an * in structures where no metal is present. (C) The G223W

37

795 structure revealed an outward-facing conformation with the physiological substrate Mn^{2+} (magenta
796 sphere) bound at the bottom of a substantial extracellular aqueous cavity (red mesh). All structures
797 are viewed from within the membrane. (D) The complete Nramp transport cycle likely consists of
798 at least six distinct conformational states. Including the structures of *S. capitis* (Sca) (Ehrnstorfer
799 et al., 2014) and *E. coleocola* (Eco) (Ehrnstorfer et al., 2017) homologs, we now have structures
800 of five of these conformations. (E) Pairwise RMSD values for the superposition of the 355 Cα
801 atoms present in all three DraNramp structures, and ScaNramp and EcoNramp. G223W
802 superimposes best with the outward-facing EcoNramp, validating our mutagenesis strategy to
803 obtain an outward-open conformation. G45R superimposes better with the inward-facing Patch
804 mutant than outward-facing G223W, suggesting it represents an inward-occluded conformation.
805 (F) Superposition of Patch mutant (gold, gray, and blue) and G45R (cyan) and (G) RMSD
806 calculated at each Cα. These structures superimpose well except for TM1a. (H) Superposition of
807 G223W (gold, gray, and blue) and G45R (cyan) and (I) RMSD calculated at each Cα. The most
808 significant rearrangements involve TMs 1b, 4, 5, 6a, and 10. In panels G and I, black lines indicate
809 average RMSD for each TM, with TMs 1, 6, and 10 divided into two halves. In panels F and H,
810 the central view is rotated 45° along the vertical axis from the view in panels A-C, while the left
811 and right views are 90° rotations of that central view. See also Figure 2—figure supplements 1 and
812 2.
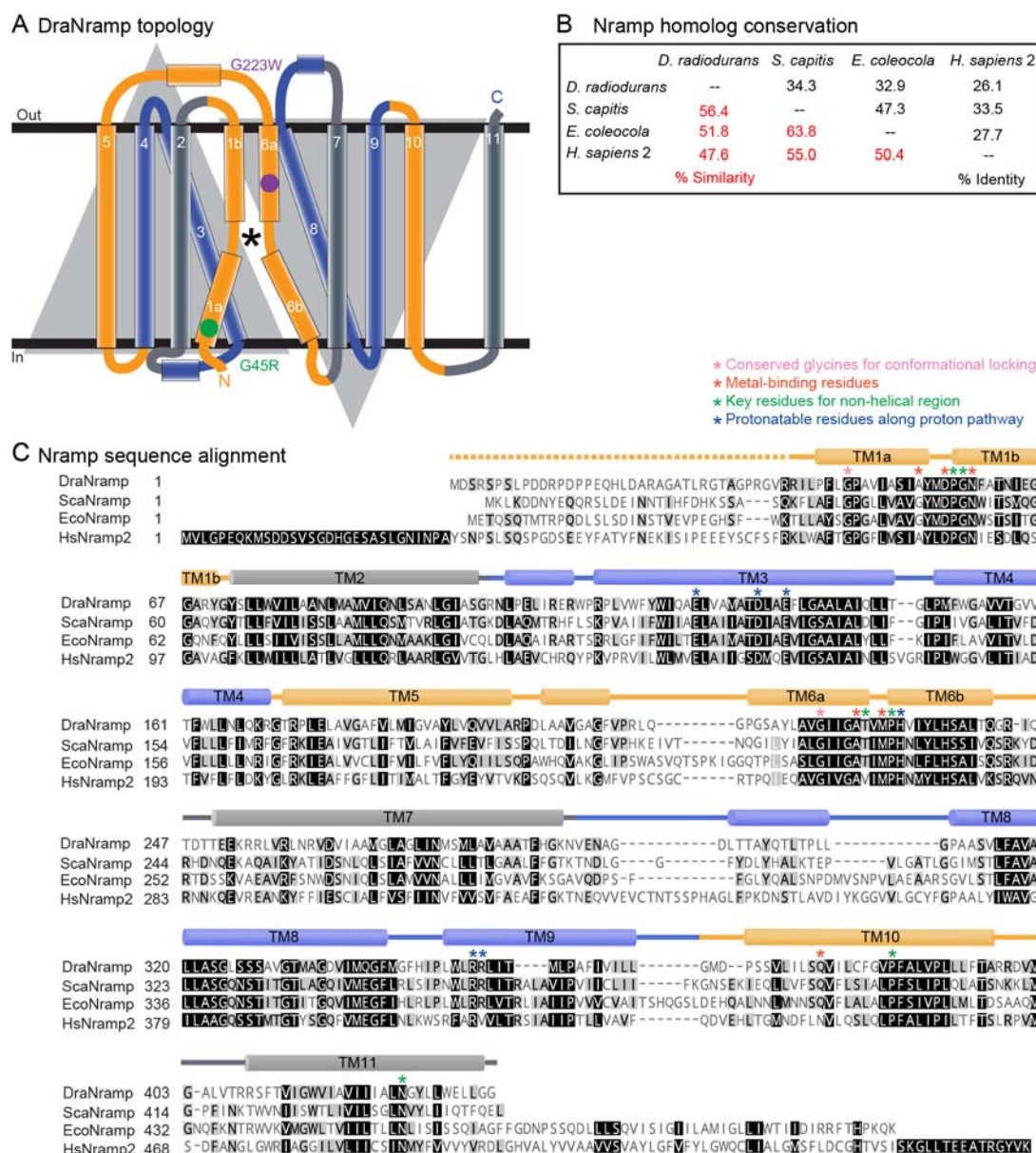
Figure 2—figure supplement 1. Secondary structure and primary sequence of DraNramp.
(A) DraNramp consists of 11 TMs, with the first ten TMs arranged in the canonical LeuT-fold: two pseudosymmetric inverted repeats of five TMs intertwine in the tertiary structure. The two conformational-locking mutations, G45R and G223W, on TMs 1a and 6a respectively, are at analogous positions within each repeat. The first and last TM in each repeat (1 and 5, and 6 and 10; gold) move significantly between the G223W and G45R structures, while the middle three remain relatively stationary (2-4, and 7-9; gray or blue). TMs 1, 4, 5, 6, and 10 group into a mobile domain, with the remaining six TMs considered a scaffold domain. * denotes the metal-binding site. (B) Sequence identity and similarity of DraNramp with *S. capitis* (Sca) and *E. coleocola* (Eco) Nramp homologs, which have been crystallized in the inward-facing[24] and outward-facing states[31] respectively, and human Nramp2 (DMT1). Sequences were aligned using the BLOSUM62 matrix, with a cutoff of 1 used for the reported % similarity. (C) Sequence alignment of DraNramp, ScaNramp, EcoNramp, and HsNramp2 shows high conservation at positions of apparent structural significance and demonstrated functional importance.

39
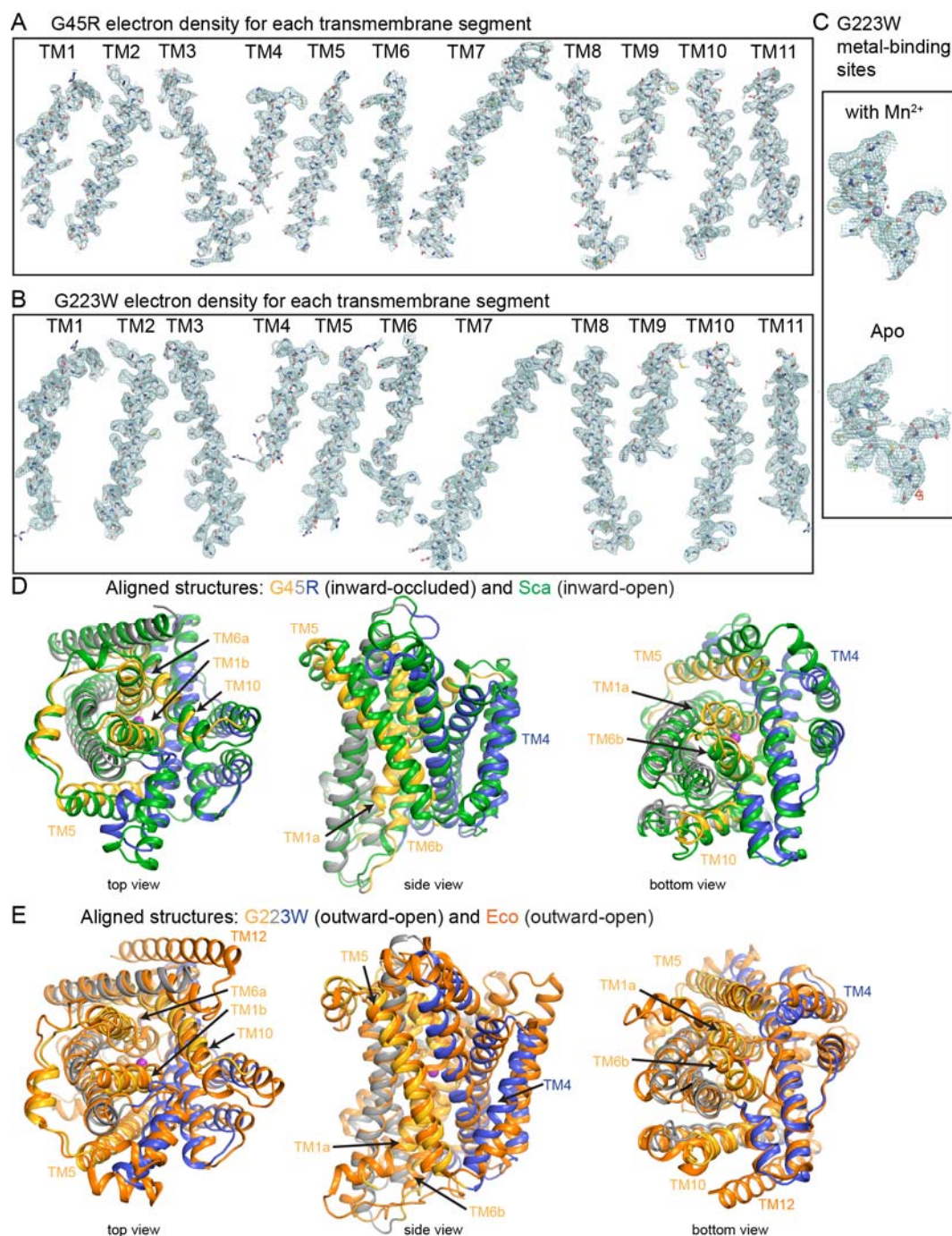
828
Figure 2—figure supplement 2. Electron density maps for new crystal structures and structural comparisons to other Nramp homologs.

831 $2F_o\text{-}F_c$ electron density maps for each transmembrane segment of (A) G45R (6C3I) and (B)
832 G223W (6BU5) structures contoured at 1.0 σ. (C) Electron density maps for the metal-binding site
833 for the Mn^{2+}-bound (6BU5) and apo (6D91) structures, with the latter also showing the $F_o\text{-}F_c$
834 difference maps contoured at +/- 3.0 σ (green/red). Superpositions of (D) G45R with ScaNramp
835 (green) and (E) G223W with EcoNramp (orange) confirm that our new structures represent
836 outward-open and inward-occluded conformations, respectively. The views in (D) and (E) are
837 based on a superposition of the G45R and G223W structures.

40

838   **Figure 2-source data 1. Nramp sequence alignment.**
839   Alignment of 6878 Nramp sequences generated with HMMER and filtered to contain only
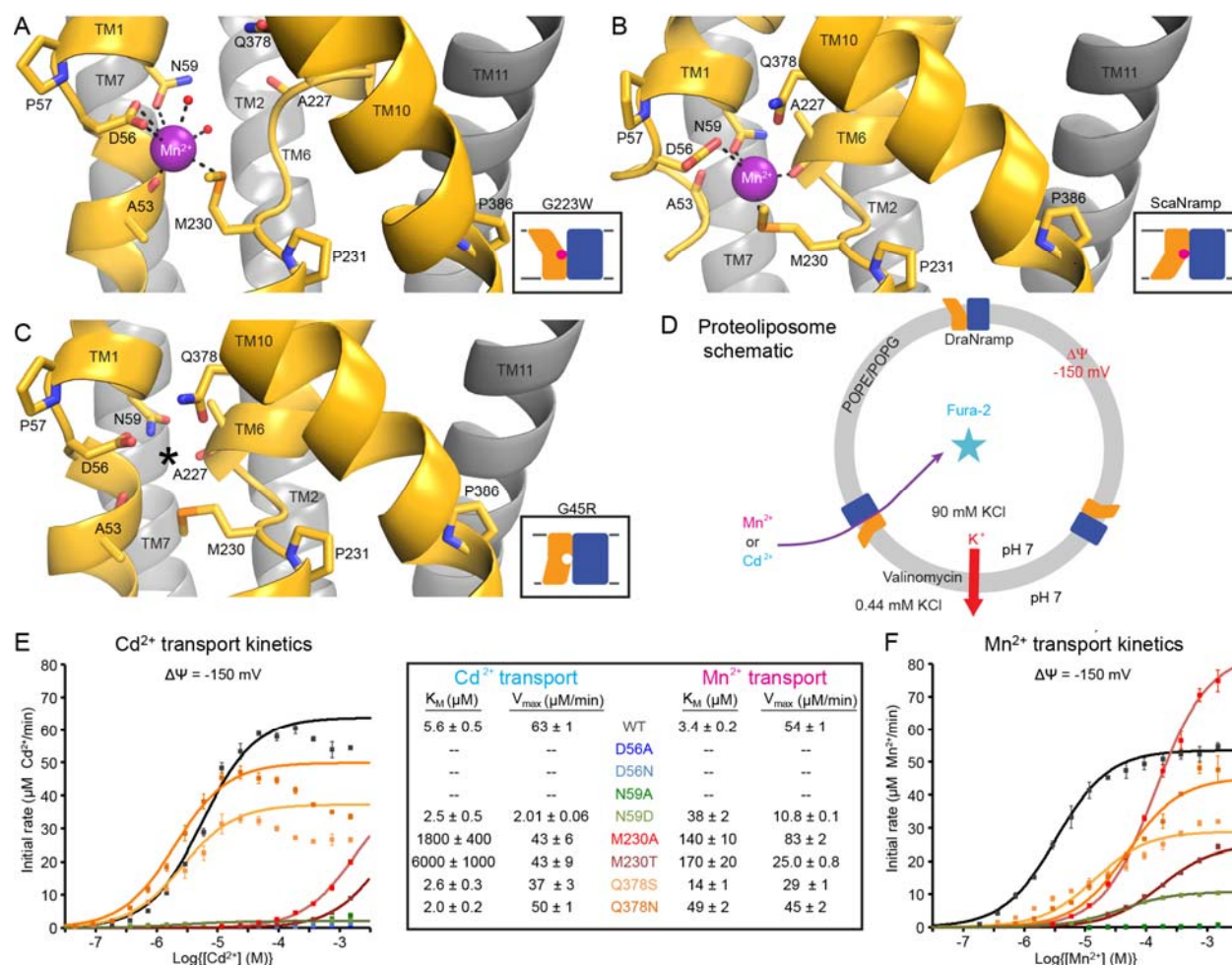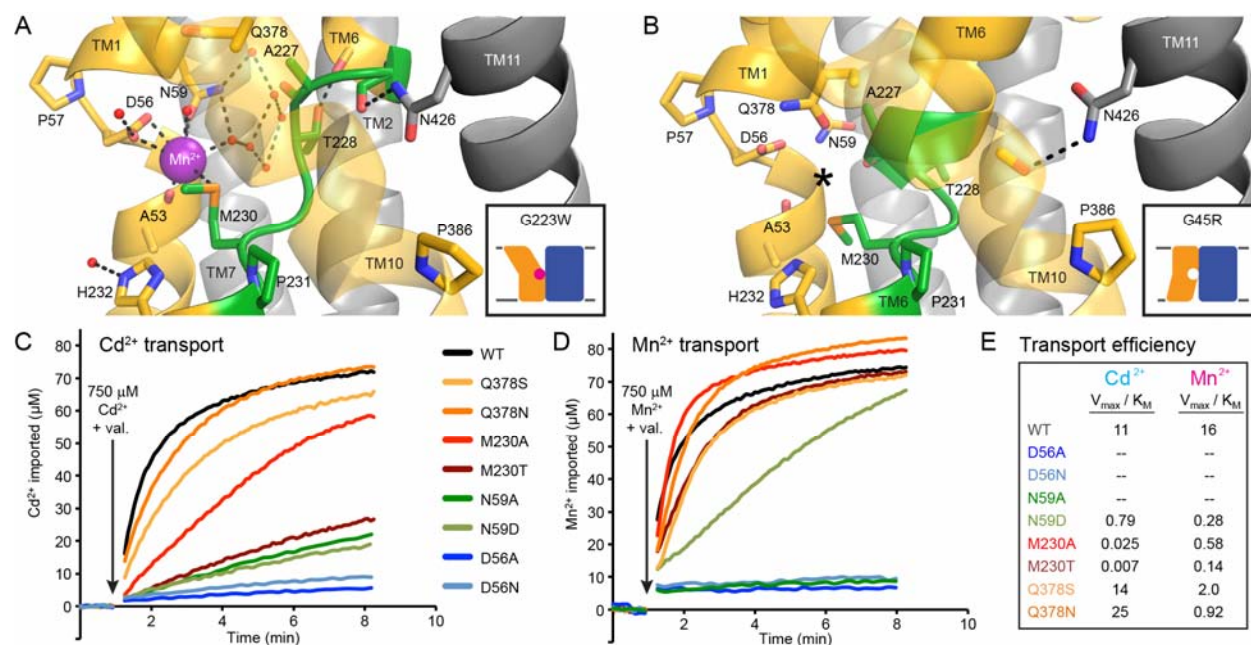840   sequences with canonical Nramp TM1 "DPGN" and TM6 "MPH" motifs.

841
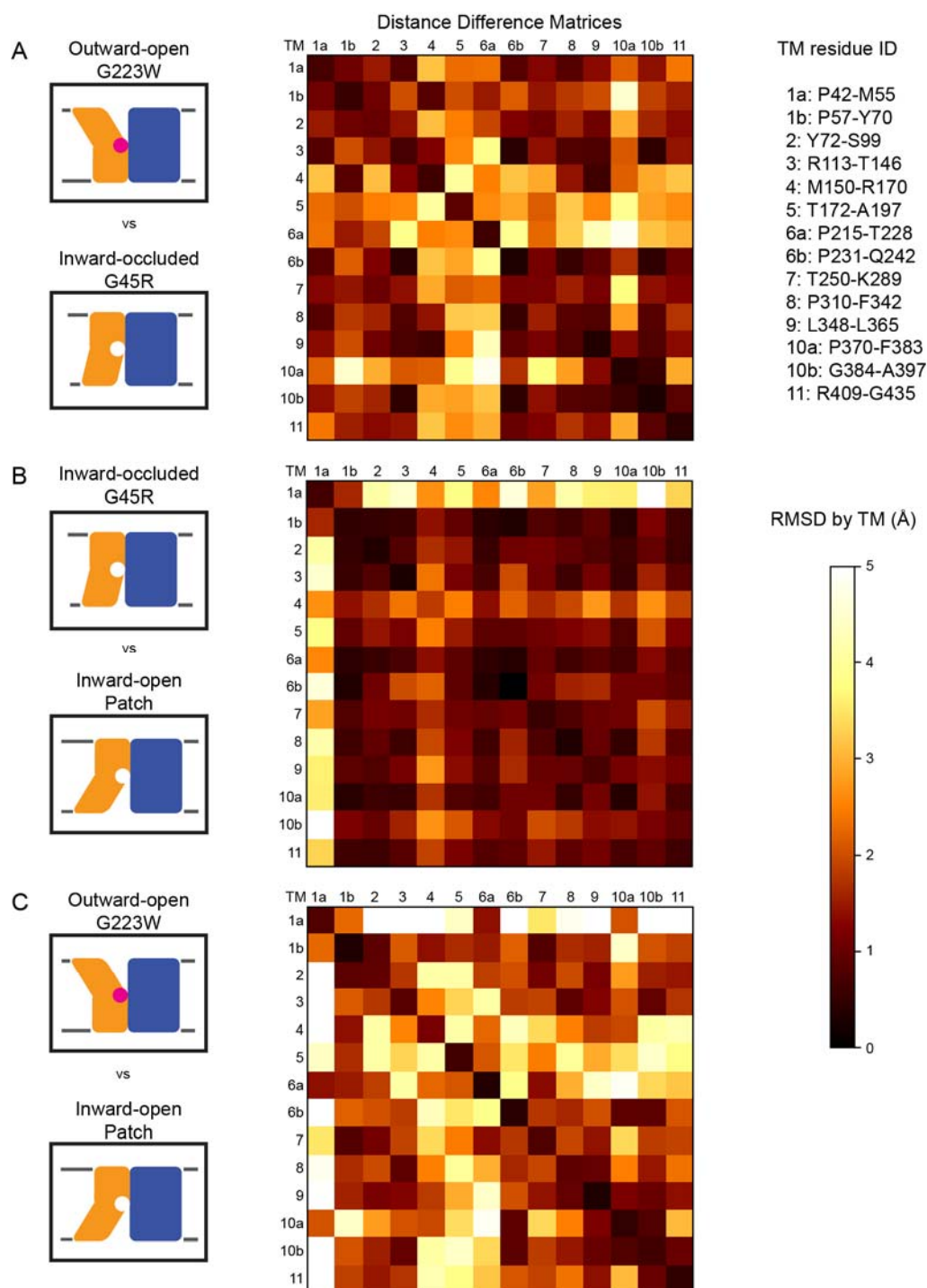
842
Figure 3. Distance difference matrices illustrate internal rearrangements during DraNramp conformational change.
We calculated the pairwise $C\alpha - C\alpha$ distances to obtain a 398 x 398 distance matrix for each of the three DraNramp structures. To compare two structures, we generated distance difference matrices(Richards and Kundrot, 1988), subtracting one distance matrix from the other. To simplify the data and focus on relative movements between helices, we then calculated the root-mean-squared deviations of submatrices, grouping residues within each helical segment. We used a total

850   of 14 segments (top right), breaking TMs 1, 6, and 10 into two separate segments before and after
851   their helix-breaking elements. The resulting 14 x 14 matrices compare (A) outward-open G223W
852   and inward-occluded G45R, (B) inward-occluded G45R and inward-open Patch mutant, and (C)
853   outward-open G223W and inward-open Patch mutant. Pairs of helices that remain stationary
854   relative to each other have RMSD values close to 0 indicated by darker colors. In contrast, pairs
855   of helices that rearrange significantly relative to each other have larger magnitude values indicated
856   by lighter coloring in the heat map. These matrices show that (A) TMs 1b, 4, 5, 6a, and 10a undergo
857   the greatest displacement relative both to the rest of the protein and to each other in the
858   conformational change from inward-occluded to outward-open. (B) In contrast, the conformational
859   change from inward-open to inward-occluded consists primarily of the large displacement of
860   TM1a, with the rest of the protein remaining mainly stationary. (C) The comparison of the
861   outward-open and inward-open states is essentially a sum of the two previous comparisons, with
862   the large TM1a displacement added to the significant movements of TMs 1b, 4, 5, 6a, and 10a.

863

864 **Figure 4. Metal-coordinating interactions vary across conformational states.**
865 (A) In the G223W outward-facing structure D56, N59, M230 and the A53 carbonyl, along with
866 two water molecules, coordinate Mn^{2+}. (B) In the inward-facing ScaNramp structure (PDB: 5M95,
867 DraNramp residue numbering) D56, N59, M230, and the A227 carbonyl coordinate Mn^{2+}. (C) In
868 the G45R inward-occluded structure D56, N59, M230, Q378, and the A53 and A227 carbonyls
869 are all close, suggesting that all six could simultaneously coordinate the metal substrate in a
870 hypothetical similar Mn^{2+}-bound conformation. Three conserved helix-breaking prolines on TM1
871 (P57), TM6 (P231), and TM10 (P386) confer the flexibility needed for the metal-binding site. The
872 TM6 unwound region is extended in the outward-open state, while TM10 bends more dramatically
873 at P386 in the inward-oriented states to close outside access to the metal-binding site. For clarity,
874 TMs 3, 4, 5, 8, and 9 are omitted in panels A-C. (D) Schematic for liposome transport assay to
875 measure Mn^{2+} or Cd^{2+} uptake. (E-F) Plots of initial rates vs. (E) Cd^{2+} or (F) Mn^{2+} concentration
876 used to determine Michaelis-Menten constants (Table inset) for WT DraNramp and binding-site
877 mutants. All mutants significantly impaired Mn^{2+} transport at lower $[Mn^{2+}]$, while only Q378
878 mutants did not severely impair Cd^{2+} transport. Data are averages ± S.E.M. (n = 3); errors on K_M
879 and V_{max} reflect uncertainty of the fit (shown as solid lines on the graphs) to the data. See also
880 Figure 4—figure supplement 1.

Figure 4—figure supplement 1. Extended TM6 unwound region enables metal-binding in outward-facing DraNramp.
(A) TM6 unwinds in the outward-facing G223W structure (non-helical region encompassing residues 226-231 is shown in green). Conserved sidechains on TM6 (T228) and TM11 (N426) donate hydrogen bonds to backbone carbonyls on TM6a to stabilize the extended non-helical region. A network of ordered water molecules forms the outer coordination sphere for the bound Mn^{2+} and extends into the outward metal-permeation pathway between TMs 1b, 6a, and 10. Conserved H232 below the metal-binding site also coordinates an ordered water. (B) For comparison the same region is highlighted in green in the G45R inward-occluded structure, although the TM6a helix is extended, and only residues 228-231 are unwound. Interestingly, in this structure the N426 sidechain donates a hydrogen bond to satisfy the backbone carbonyl on TM10 just above the conserved P386. For clarity, TMs 3, 4, 5, 8, and 9 are omitted and TM10 is shown as a transparent ribbon in panels A and B. (C-D) Representative traces (n = 3) for WT and binding-site mutants (C) Cd^{2+} and (D) Mn^{2+} uptake at 750 μM. Mutations to D56 eliminate all metal transport, while mutations to N59 severely impair transport for both metals. At higher metal concentrations, mutations to M230 are much more deleterious to Cd^{2+} transport than Mn^{2+} transport, while mutations to Q378 do not greatly impair transport of either metal. (E) Transport efficiency (V_{max}/K_M) comparisons from the data in Figure 3E-F illustrate all tested mutations are deleterious to Mn^{2+} transport, while all but Q378S and Q378N are deleterious to Cd^{2+} uptake.

45
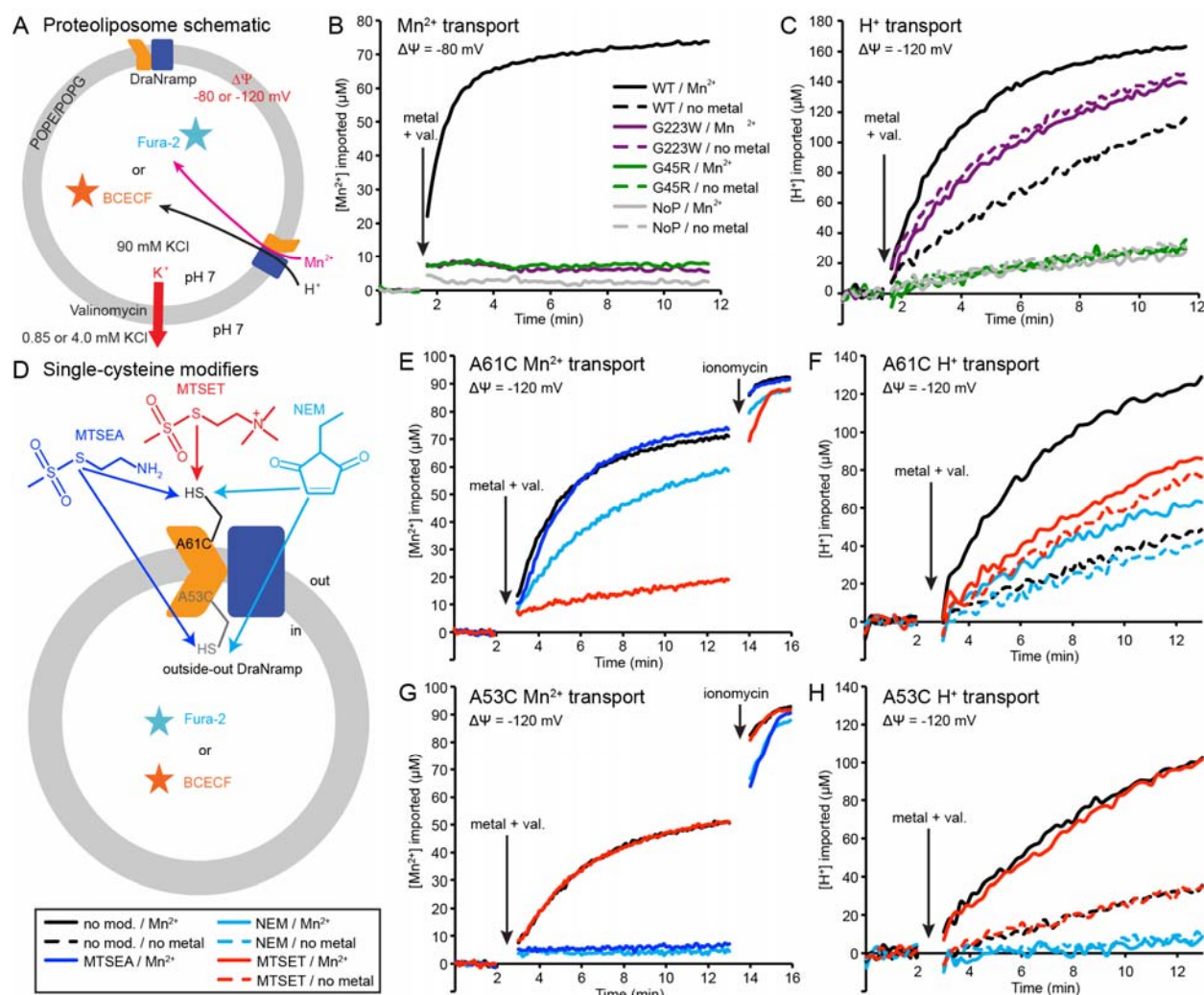
Figure 5. Outward-locked mutants retain H⁺ transport ability.
(A) Proteoliposome assay schematic for monitoring M^{2+} and H^+ import. Membrane potential ($\Delta\Psi$) was established using K^+ gradients and valinomycin. (B) Mn^{2+} uptake over time; WT enabled robust uptake while G45R and G223W showed no activity. NoP = No Protein control liposomes. (C) H^+ uptake over time; WT enabled significant H^+ uptake without metal (H^+ uniport), further stimulated by Mn^{2+}. G223W showed a larger H^+ uniport rate, but Mn^{2+} provided no enhancement; G45R showed no H^+ transport activity. Traces are representative of four experiments. (D) Schematic for *in vitro* cysteine modification of A53C (inside accessible) and A61C (outside accessible). MTSEA and NEM are membrane permeable, whereas permanently-charged MTSET is not. (E,G) Mn^{2+} and (F,H) H^+ transport over time in the presence or absence of cysteine modifying agents. Adding ionomycin allows divalent cation entry to achieve maximum signal. Traces are representative of three experiments. See also Figure 5—figure supplement 1.

46
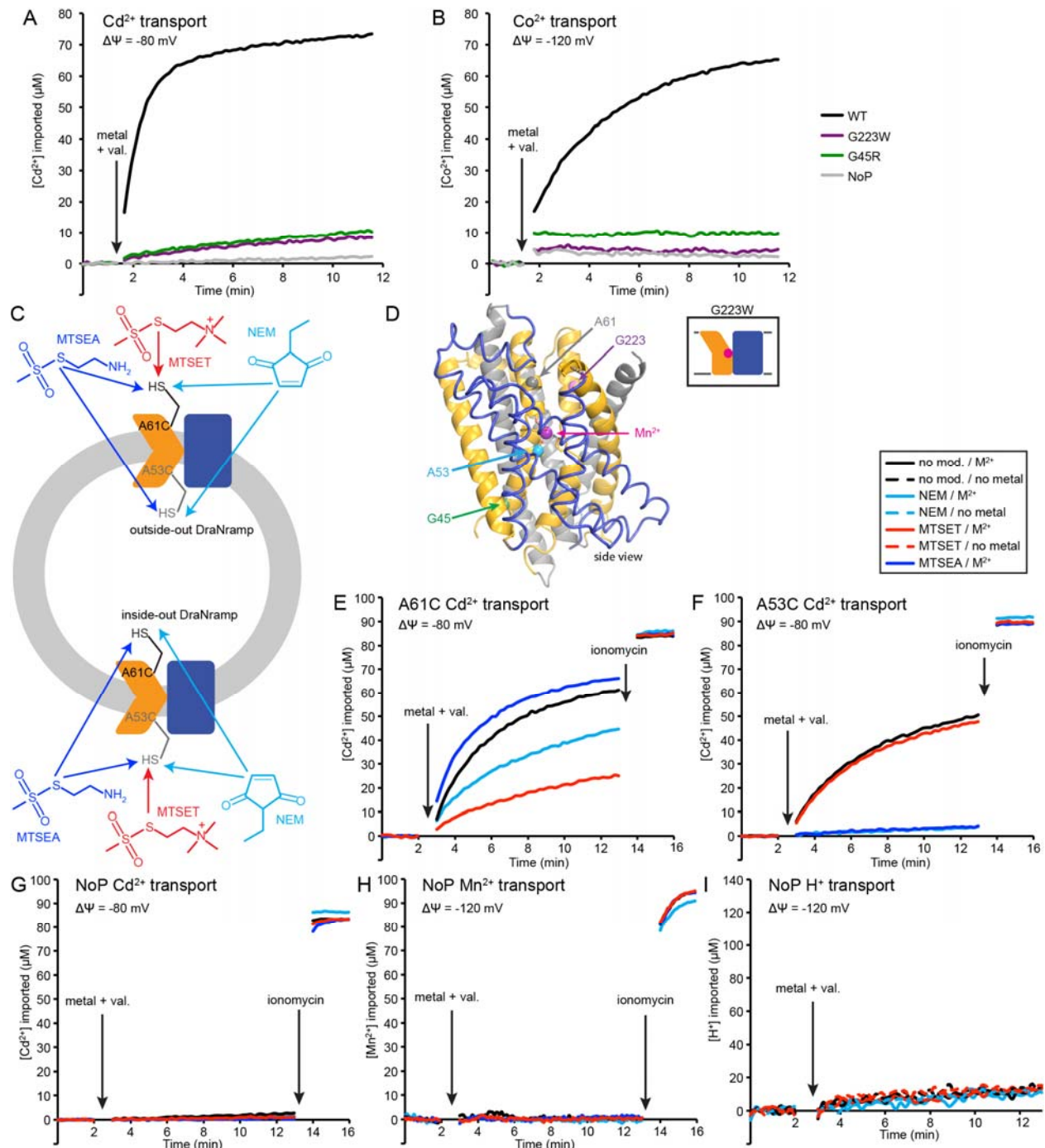
914
915 **Figure 5—figure supplement 1. Conformational locking impairs metal transport.**
916 Sample traces (n=4) of (A) Cd^{2+} and (B) Co^{2+} transport over time in proteoliposome. WT enabled
917 robust uptake while G45R and G223W did not. NoP = No Protein control liposomes. (C)
918 Schematic for *in vitro* cysteine modification of A53C (inside accessible) and A61C (outside
919 accessible). Assuming random insertion into liposomes, there is a ~50:50 mix of right-side-out and
920 inside-out transporters. A53C and A61C should thus be fully-labeled by membrane-permeable
921 MTSEA and NEM for transporters in both orientations. In contrast, only right-side-out A61C and
922 inside-out A53C transporters should be labeled with the membrane-impermeable MTSET. (D)
923 A61 and G223 line the metal permeation pathway to binding site, while A53 and G45 face the

924   metal exit pathway to the cytoplasm. (E,F) Sample traces (n = 3) of Cd^{2+} transport over time in the

925   presence or absence of cysteine modifying agents, with trends similar to Mn^{2+} transport in Figure

926   5E,G: (E) MTSET greatly reduced A61C Cd^{2+} transport, NEM had a moderate effect, and MTSEA

927   had a slight enhancing effect; (F) NEM and MTSEA eliminated A53C Cd^{2+} transport, while

928   MTSET had no effect. (G-I) Sample traces (n = 3) show that none of the modifiers enabled M^{2+} or

929   H^+ leak into empty liposomes.
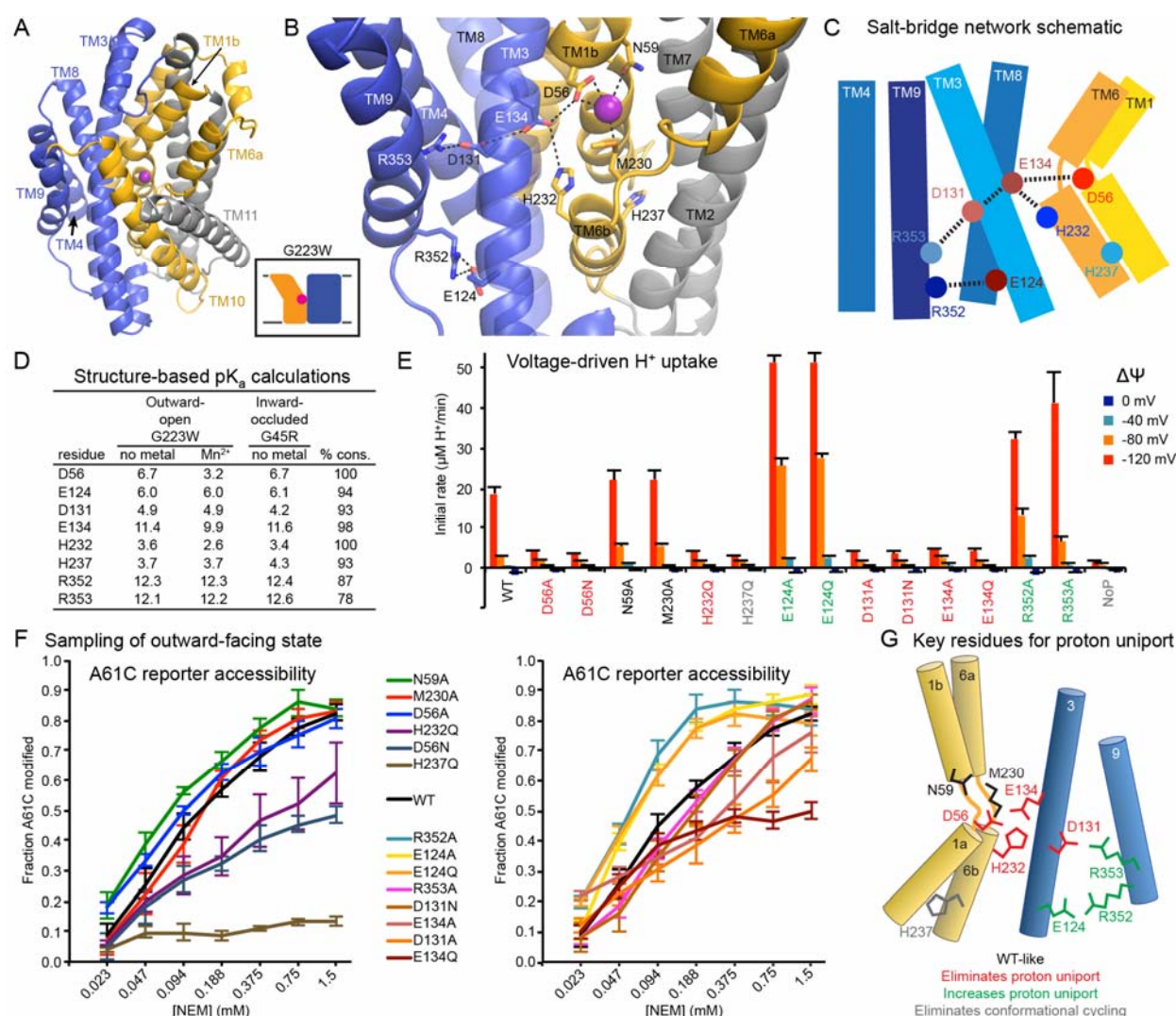
Figure 6. Conserved salt-bridge network provides pathway for proton uniport.
(A) View from an angle above the membrane looking down into the extracellular aqueous cavity in the outward-facing G223W structure. (B) Zoomed-in view (with TM10 and TM11 omitted for clarity) and (C) schematic showing a network of conserved protonatable residues that originates from the metal-binding site and extends into the cleft between TMs 3, 4, 8, and 9. H232 and E134 abut metal-binding M230 and D56, providing a connection to the D131-R353 and R352-E124 salt-bridge pairs. (D) pK$_a$ estimates by PROPKA (Dolinsky et al., 2004) from high-resolution DraNramp structures. (E) Initial rates of basal H$^+$ uptake at various ΔΨs (averages ± S.E.M.; n ≥ 4). Mutations to D56, E134, H232, and D131 eliminated H$^+$ uniport observed for WT. N59 and M230 mutants retained significant H$^+$ uptake. Mutations to E124, R352, and R353 enhanced H$^+$ uniport. (F) Dose-response curve of outward-facing reporter A61C modification versus NEM concentration. All mutants except H237Q sampled the outward-facing state, which is required for H$^+$ transport to occur (Figure 5). Data are averages ± S.E.M. (n ≥ 3). (G) Salt-bridge network schematic shows clustering of four residues required for H$^+$ uniport (red) as well as three residues that may restrain this flux (green). See also Figure 6—figure supplement 1.

49
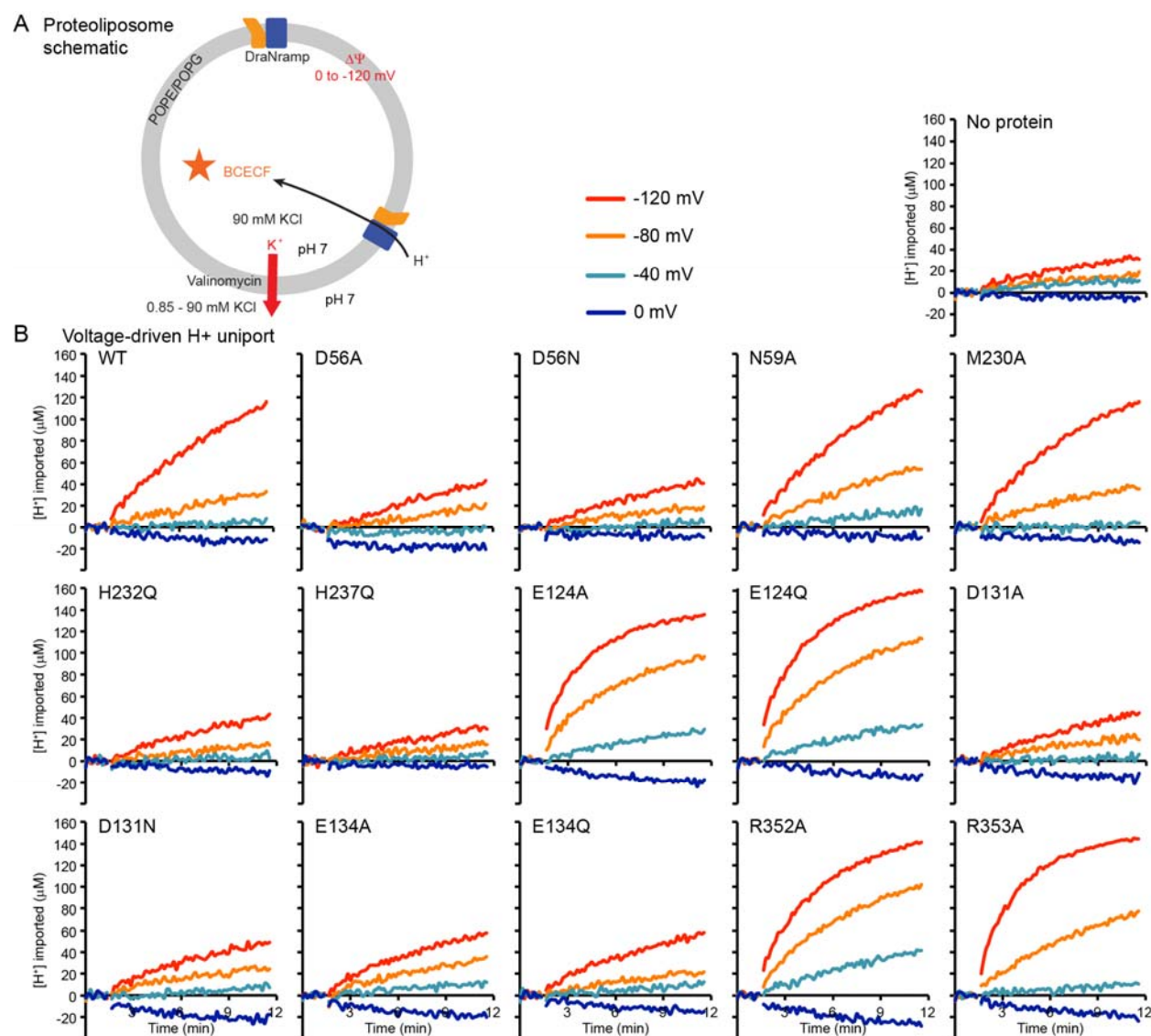
Figure 6—figure supplement 1. Sample traces illustrate mutant perturbations of voltage-driven proton uniport.

(A) Schematic for proteoliposome proton uptake assay. (B) Representative time traces (n ≥ 4) of H$^+$ uptake into liposomes measured at four $\Delta\Psi$ values for each mutant or no-protein control.

50
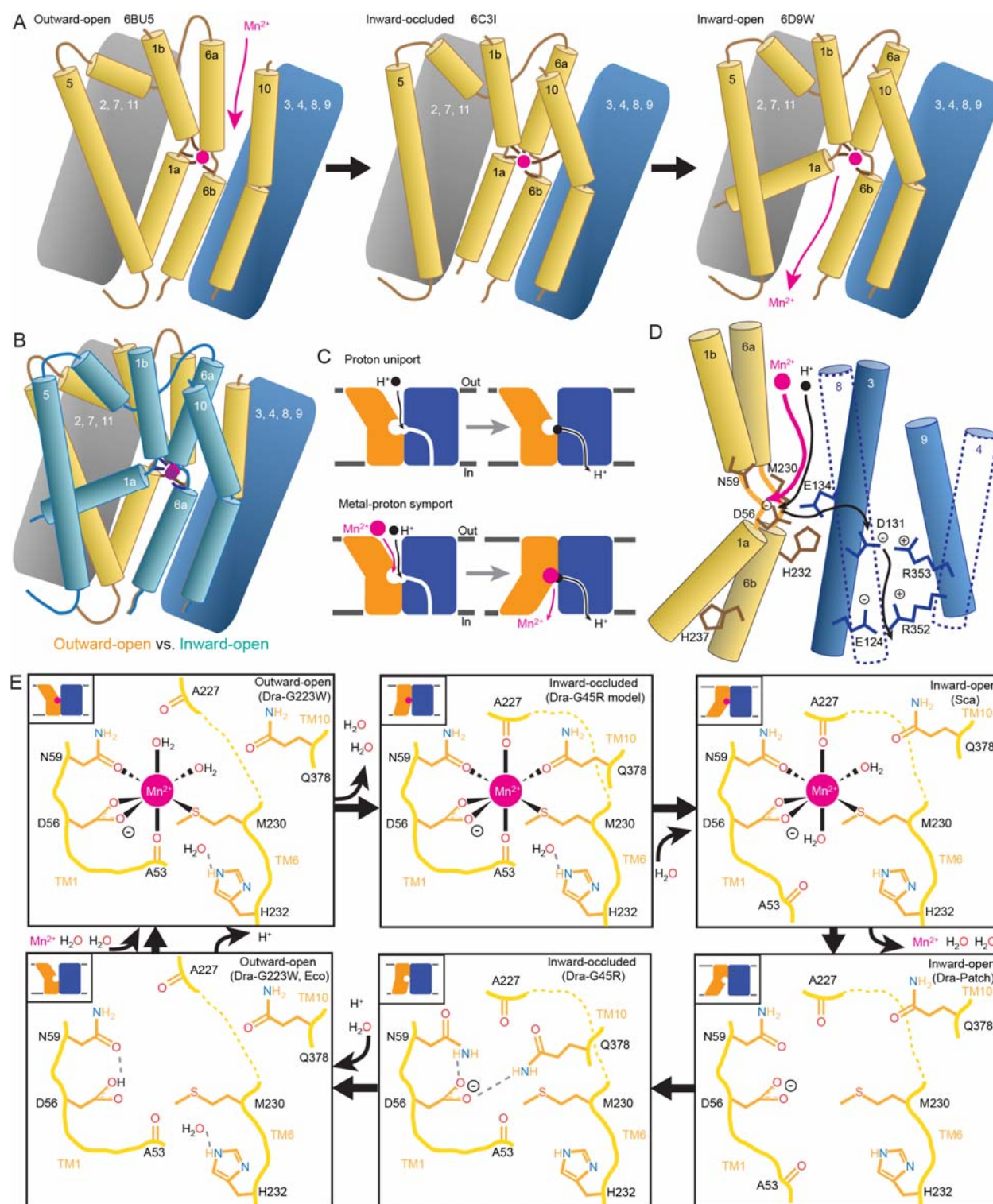
Figure 7. Mechanistic models for conformational change, proton transport, and metal transport.

(A) Model of conformational change: The metal ion reaches the outward-facing binding site via the vestibule between TMs 1b, 6a, 10, 3, and 8. TM6a and 10 bend inward to close the vestibule in the inward-occluded conformation. TM6a's inward bend pulls on TM5 via extracellular loop 5-

957 6 to initiate opening of the inner gate. Finally, TM1a swings away from TM6b to open the
958 intracellular vestibule into which the metal diffuses. (B) Superposition of outward- (gold) and
959 inward-facing (teal) conformations illustrate key movements by TMs 1, 5, 6, and 10. (C) Overall
960 transport model: While metal transport requires complete conformational cycling, proton uniport
961 occurs through the outward-facing state. (D) Proton transport model: A proton transits the external
962 vestibule to reach the binding site near the membrane center and initially binds to D56. Metal
963 enters through the same passageway, ejecting the proton, which then passes to D131, with H232
964 and E134 facilitating the transfer. The proton ultimately reaches the cytoplasm through the polar
965 network between TMs 3, 4, 8, and 9, while the metal must await a bulk conformational change
966 that opens a separate pathway between TMs 1a, 2, 5, 6b, 7, and 8. Proton uniport follows the same
967 route, with the D56-D131 transfer occurring at a slower rate without metal substrate. (E) Model
968 for metal coordination during the transport process: The metal initially binds in the outward-facing
969 state to D56, N59, M230 sidechains and the A53 carbonyl, shedding all but two water ligands. As
970 the outward metal-permeation pathway closes, Q378 and the A227 carbonyl displace the waters
971 so that the metal is fully coordinated by six amino acids in the occluded state. As the inner gate
972 opens, Q378 and the A53 carbonyl withdraw and are replaced by waters. The metal is then released
973 into the cytoplasmic aqueous vestibule. To facilitate the return to the outward-facing state, Q378
974 and N59 donate hydrogen bonds to negatively-charged D56 in the occluded return conformation
975 seen in our G45R structure. Finally, as the transporter returns to an outward-open state, it may bind
976 a proton in preparation for metal-binding.

52

977 **Video 1. Internal rearrangements during DraNramp conformational changes.**
978 Morph of the structure of DraNramp based on a global superimposition of the three captured
979 conformational states. TMs 1, 5, 6, and 10 are colored gold, TMs 3, 4, 8, and 9 blue, and TMs 2,
980 7, and 11 gray, viewed in the membrane plane and the intracellular face pointing down. The morph
981 starts from the G223W outward-facing conformation, transitions to the G45R occluded state, then
982 to the patch mutant inward-open state. The view then shifts to the intracellular face, followed by
983 the external face, continuing to alternate back and forth through these three conformations.